

# Three-Dimensional Phase Unwrapping for Satellite Radar Interferometry, I: DEM Generation

Batuhan Osmanoglu, Timothy H. Dixon, and Shimon Wdowinski

**Abstract**—Determining the Earth’s surface topography and deformation with interferometric synthetic aperture radar involves measurement of phase, which, for a typical coherent radar signal, can only be done modulo  $2\pi$ . The cycle of ambiguity inherent in the phase measurement has to be unwrapped over all observation dimensions (e.g., azimuth, range, and time) to remove the  $2\pi$  ambiguity of the phase measurements. For a time series of SAR images, useful for reducing noise in topographic applications or measuring time-varying surface deformation, the necessary steps to connect ambiguous radar phase measurements are more challenging, and the operation may be termed 3-D phase unwrapping. We describe a 3-D unwrapping approach using an extended Kalman filter. Our approach readily exploits existing information, and is robust in the presence of noise. For all tested data sets, it provides improved accuracy compared to existing approaches.

**Index Terms**—Digital elevation models, kalman filters, radar interferometry, synthetic aperture radar.

## I. INTRODUCTION

INTERFEROMETRIC synthetic aperture radar (InSAR) has been in use since the 1970s, with scientific applications that include topographic mapping and measurement of surface deformation [1]–[8]. Early topographic applications used interferometric fringe lines as isoheight contours, resulting in relatively low resolution topographic information [1]. However, current techniques for generating high-resolution digital elevation models (DEMs) calculate the height value for each point in the image. DEM generation and surface deformation measurements both require resolving the interferometric phase ambiguity, an operation known as phase unwrapping. In many cases, parts of the interferogram will be decorrelated because of a combination of error sources, making unwrapping difficult [9]. It is possible, however, to combine independently generated interferograms, reducing the effect of such errors.

For DEM generation, a simple weighted average of independent DEMs is not an optimal solution to the noise and decorrelation problem, as it underestimates the spatio-temporal variability in the noise terms [10]. Although there are several

published approaches to this problem, they all have disadvantages in the presence of noise or areas of low coherence [10]–[16]. In this paper, we present a novel method for generating DEMs, combining multiple SAR acquisitions using an extended Kalman filter (EKF). The EKF incorporates noise filtering, unwrapping, and topography calculation in a single operation. The input data consists of interferograms created with different spatial baselines and short temporal separations. These data are termed 3-D because they consist of a stack of 2-D spatial images. In other words, in addition to the two spatial dimensions of the interferogram, the stack forms the third dimension, which can be time for deformation analysis, or perpendicular baseline for topography.

The main objective of this paper is the development of a 3-D unwrapping technique combining observations from multiple information sources (e.g., interferograms, existing low-resolution DEMs) to generate a new DEM that is significantly more accurate than any of the input data alone. Our technique can be readily extended to measurement of surface deformation where the deformation can be assumed constant in time, or can otherwise be characterized by a simple model of time variation. This paper focuses on the development of the Kalman-based unwrapping algorithm, but includes some comparison with other algorithms for DEM generation. A broader comparison with other nonlinear filters for DEM generation will be the focus of separate studies.

This paper is organized as follows. Section II describes the technical requirements for 3-D unwrapping and previous work. Section III describes the EKF, and the proposed method for DEM calculation. Section IV applies the EKF to synthetic data, C-band (Envisat) data and X-band (TerraSAR-X) data, and contrasts the results with independent, comparable-resolution DEMs. For all data sets, weighted average DEMs using conventional unwrapping methods, as well as a maximum-likelihood (ML) estimator after Eineder and Adam [13] are also calculated. We then compare the performance of our EKF with other available DEMs in Section V.

## II. TECHNICAL BACKGROUND

Several algorithms are developed for time series analysis of InSAR data: PSInSAR [17], [18]; PSI [19], [20]; SBAS [21]–[23]; StaMPS [24]; and SqueeSAR [25]. All these approaches aim to connect ambiguous phase measurements to produce a near continuous record of displacement, even though unwrapping is achieved by a series of spatial and temporal

Manuscript received May 13, 2011; revised November 27, 2012; accepted January 15, 2013. Date of publication April 30, 2013; date of current version December 12, 2013.

B. Osmanoglu is with the Geophysical Institute University of Alaska–Fairbanks Fairbanks, AK 99775 USA (e-mail: batu@rsmas.miami.edu).

T. H. Dixon is with the Department of Geology, University of South Florida, Tampa, FL 33620 USA (e-mail: thd@usf.edu).

S. Wdowinski is with the Marine Geology and Geophysics RSMAS–University of Miami Key Biscayne, Miami, FL 33149 USA (e-mail: swdowinski@rsmas.miami.edu).

Color versions of one or more of the figures in this paper are available online at <http://ieeexplore.ieee.org>.

Digital Object Identifier 10.1109/TGRS.2013.2247043

operations. Previous approaches to the 3-D phase connection (unwrapping) problem include applications in InSAR and magnetic resonance imaging [26]–[35]. Multidimensional unwrapping is a challenging problem and the previous studies have both advantages and disadvantages depending on the application, noise level and phase gradients. Our study approaches this problem in a different way and we believe significant benefits in terms of flexibility, treatment of noise, and the ability to constrain the solution with external information.

DEM reconstruction using multibaseline (multichannel) SAR interferometry is demonstrated using several methods, including wavelets [10]; ML techniques [13], [14], [36]–[38]; and maximum *a posteriori* estimation techniques [12], [15], [39], [40]. The shuttle radar topography mission (SRTM) generated DEMs by unwrapping the interferogram and multiplying the observed phase values with a height-to-phase conversion factor, which is a function of the baseline. The unwrapping is achieved using a connected component variant of the standard branch-cut algorithm [3], [41].

Interferometric SAR measurements are sensitive to range change in the line-of-sight direction. Assuming the scattering phase is the same for the master (initial) pass and slave (interferometry) pass, and ignoring any changes in atmospheric phase delays, the phase change between the two SAR acquisitions can be related to two-way range change in the line-of-sight direction [42], [43]

$$\Delta\phi = \frac{2\Delta R}{\lambda/2\pi} \quad (1)$$

where  $\Delta\phi$  is the phase change,  $\Delta R$  is the range difference between acquisitions, and  $\lambda$  is the radar wavelength. Equation (1) shows that when  $\Delta R$  is  $\lambda/2$ ,  $\Delta\phi$  will be equal to  $2\pi$ . Any further changes in the range direction become ambiguous, because the phase is observed between  $-\pi$  to  $\pi$  and wraps around such that  $\Delta\phi = \Delta\phi + 2\pi$ . This wrapping behavior of phase observations generates contours (fringe lines) where the phase changes from  $-\pi$  to  $\pi$ . Assuming all the range change is because of topography, the height change that will correspond to a  $2\pi$  phase change is [42], [43]

$$z_{2\pi} = \frac{\lambda R \sin(\theta)}{2B_{\perp}} \quad (2)$$

where  $z_{2\pi}$  is height ambiguity,  $\lambda$  is wavelength,  $R$  is the range between target and satellite's position during master acquisition,  $\theta$  is the antenna look angle, and  $B_{\perp}$  is the perpendicular baseline. As seen from (2), the height ambiguity and perpendicular baseline are inversely proportional, i.e., an increasing perpendicular baseline decreases the height ambiguity. Therefore, interferograms with short perpendicular baselines contain less topographic fringes (and details), thus simplifying the unwrapping process, whereas large perpendicular baselines increase the sensitivity of the measurement to topography, providing more detailed observations but at the expense of more difficult unwrapping. The measurement sensitivity is indicated by the height-to-phase conversion factor, defining phase change for a unit of elevation change [41], [44]

$$\frac{\Delta\phi}{\Delta z} = \frac{2\pi}{z_{2\pi}} = \frac{4\pi}{\lambda} \frac{B_{\perp}}{R \sin(\theta)} \quad (3)$$

where  $\Delta\phi/\Delta z$  is the height-to-phase conversion factor. This relationship between perpendicular baseline and radar measurements of topography enables us to obtain a highly accurate DEM through the use of EKF.

For DEM generation the effect of orbital errors are inversely proportional to the perpendicular baseline. Therefore a minimum value for the perpendicular baseline can be calculated based on the required DEM accuracy as shown in [43]

$$B_{\perp\min} = \frac{\varepsilon_{B_{\perp}}}{\varepsilon_{\text{DEM}}} |Z| \quad (4)$$

where  $B_{\perp\min}$  is the minimum perpendicular baseline,  $\varepsilon_{B_{\perp}}$  is the orbital error in the perpendicular baseline component,  $\varepsilon_{\text{DEM}}$  is the requested DEM accuracy for the end product, and  $|Z|$  is the absolute height variation in the mapped area. Similarly, an upper limit for the perpendicular baseline comes from the critical baseline, after which interferograms are decorrelated [43]

$$B_{\perp\text{crit}} = \lambda \frac{W_R}{c} R_1 \tan(\theta - \alpha) \quad (5)$$

where  $B_{\perp\text{crit}}$  is critical baseline,  $\lambda$  is wavelength,  $W_R$  is radar bandwidth,  $c$  is speed of light,  $R_1$  is range to first pixel,  $\theta$  is look angle, and  $\alpha$  is slope in the range direction.

The use of filter-based unwrapping methods is proposed for 2-D unwrapping of InSAR measurements [26], [45]–[49]. For 3-D unwrapping, EKFs have several advantages: first, EKFs account for measurement uncertainties, second, EKFs operate incrementally (recursively), third, there is extensive literature on nonlinear estimation of multisensor systems using EKFs [50]–[53], and fourth, EKFs can account for *a priori* information.

It is demonstrated that EKFs underestimate the error covariance when the observations are highly nonlinear and the models cannot be described with a first-order Taylor-series expansion [54]–[56]. Application of so-called unscented Kalman filters [54], [55], or particle filters [49], [57], should improve the estimation accuracy when the observations have severe nonlinearities, such as cliffs or other regions of extreme topographic gradients.

Numerous textbooks and articles provide an introduction to Kalman filters [58]–[60], [56]. Our analysis is an extension of the unwrapping algorithm developed by Krämer [45], details of which can also be found in [47] and [48]. Krämer's algorithm estimates the continuous phase values from the complex (amplitude and phase) InSAR observations, with the assumption that each observation follows a normal distribution, and a relation can be defined between the neighboring pixels in a 2-D regular lattice. In certain cases, the Gaussian assumption (normal distribution of observations) does not hold [61], [49], yet it is an assumption often made to simplify algorithm development [10], [42], [47], [62]–[64].

Kalman filters consist of two processing steps: prediction and control. During the prediction step, the next filter state along some path is calculated based on a known model. The result of the prediction step is then compared with the observation in the control step to update the predicted value and estimated error covariance. Previous studies on filter-based unwrapping algorithms focused on the use of a geometric path,

such as row- or column-order paths, and the masking of low-quality areas [47], [49]. We propose an alternative approach: following the highest-quality path and unwrapping all pixels. Following a high-quality path enables the algorithm to estimate state vector and variance matrices correctly before attempting to solve points with a lower signal to noise ratio (SNR). Because the algorithm has a higher probability of calculating a wrong estimate for low SNR points, they are set aside until the end to minimize error propagation. The highest-quality path is determined according to Fisher's Distance metric, which is a measure of phase similarity based on the Fisher's information theory [65]

$$FD_0 = \frac{1}{4N} \sum_{n=1}^N \frac{\mathcal{L}(\phi_n \phi_0^*)^2 (\sigma_{\phi_0}^2 + \sigma_{\phi_n}^2)}{\sigma_{\phi_0}^2 \sigma_{\phi_n}^2} + \log(4\pi^2 \sigma_{\phi_0}^2 \sigma_{\phi_n}^2) \quad (6)$$

where,  $FD_0$  is the Fisher's Distance for the current point calculated over its neighborhood,  $N$  is the number of neighboring pixels,  $\mathcal{L}(\phi_n \phi_0^*)$  is the complex differencing of phase angles, and  $\sigma_{\phi_0}$  is the expected standard deviation of phase values from coherence calculated after [66]. As in (6), Fisher's Distance approach compares neighboring phase values with regard to their expected phase error (based on coherence). Further details of the method are presented in [65]. It is important to separate the effects of path and unwrapping function in the selection of unwrapping path algorithm. Therefore, the comparison of Fisher's Distance to other path algorithms in [65] employed a simple (integral of phase derivative) unwrapping function. It is inevitable that the results obtained with the EKF will show some dependence on the selected path. However, these effects are minimized by constraining the filter's initial conditions with an existing DEM. In weak (or no) initial conditions, the filter can iteratively approach a solution by combining solutions obtained using different paths. In this paper, we initialize the EKF with a known DEM for real data analysis, and do not utilize any iterations over the unwrapping path.

A multibaseline InSAR data set is 3-D, e.g., azimuth, range and interferogram. The interferogram dimension can be organized in chronological order when analyzing deformation, or according to the value of perpendicular baseline when analyzing topography. An algorithm can be constructed by starting from the reference image and unwrapping the phase of neighboring pixels in all 3-D of the data set. Defining the DEM as a constant signal through time, we can assume that it is common in all interferograms. Therefore, even though interferometric pairs are acquired at different times, we can treat them as synchronous observations. There are three common methods for combining multiple observations using Kalman filters: parallel filtering, data compression filtering, and sequential filtering [Fig. 1(a)–(c)] [50], [51]. Although all these methods perform similarly for linear observations acquired using identical sensors, the parallel filter has better performance for observations with different characteristics; this is the case for wrapped topographic signal in interferograms with different baselines. The disadvantage of the parallel filter comes from the larger matrix sizes, as the filter merges all observations

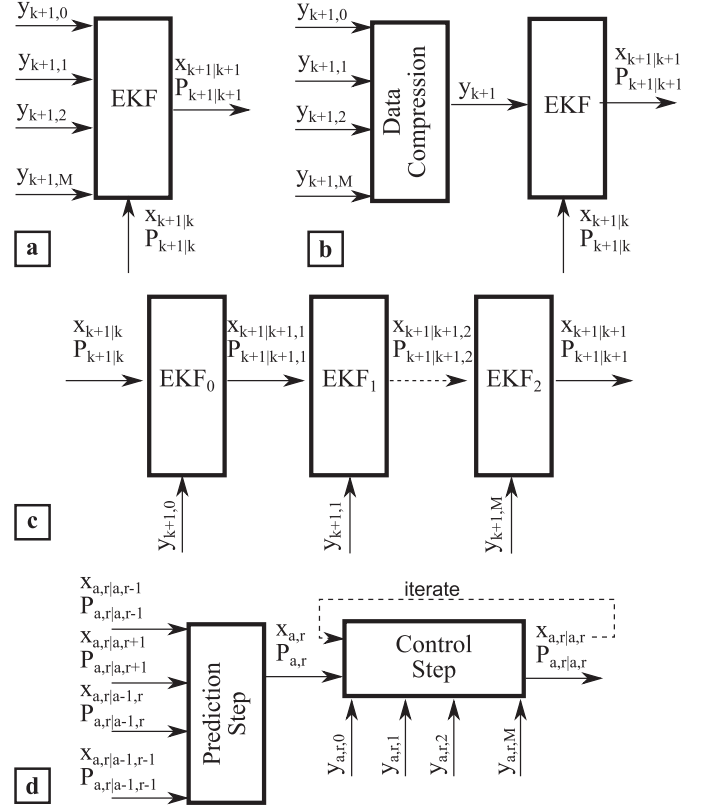


Fig. 1. Different methods to combine multiple observations with EKF. (a) Parallel filter. (b) Data compression. (c) Sequential filter.  $y$  is observation vector,  $x$  is state vector,  $P$  is error covariance, and subscripts indicate sample number  $k$ .  $x_{k+1|k}$  is state vector prediction for sample  $k+1$  given  $x_k$ . Modified from [50]. (d) Diagram of designed EKF. In prediction step,  $N$  state vectors from previously-solved neighbors are weighted and averaged into single state vector. In control step, observations from  $M$  interferograms are used to correct predicted state vector. Dashed line: iteration path for state vector ( $x$ ). Subscripts  $a, r, M$ : 3-D of data.

into a large observation vector. If all interferograms are to have the same baseline, however, then a data compression filter could prove beneficial. Because interferograms with different baselines are used in DEM generation we use parallel filtering with some additions from a data compression method in the prediction step, and also with an iterative control step, as explained in detail in Section III.

### III. EXTENDED KALMAN FILTER

We developed an EKF to unwrap 3-D, multibaseline InSAR data to obtain a DEM of the observed area. In our implementation, information from every interferogram is fed into a single filter, where interferometric phase changes are converted into height values and gradients in radar coordinates. Accordingly, each filter state consists of three elements: height relative to a reference point and gradients in the range and azimuth directions. State-space equations define the relationship between the Kalman filter states and the observations. For this paper, the topographic height and its gradient constitute the state vector. Hence, the state-space equations can be given as

$$x_0^- = DA_N x_N^+ + w_N \quad (7)$$

$$y_M = H_M(x_0^-) + v_M \quad (8)$$

where  $x_0^-$  is the state,  $D$  is the matrix of averaging coefficients,  $A_N$  is the transition matrix that relates the neighboring states to the current state,  $w_N$  is the process noise,  $y_M$  is the observation vector,  $H_M$  is the operation that links the state to the observation, and  $v_M$  is the measurement noise. In all equations, the subscript  $N$  is solved pixels in the  $3 \times 3$  neighborhood around the current point. Similarly subscript  $M$  is  $M$  interferograms (or observations).

Each term of the (7) and (8) is a matrix and are further explained between (9) and (15). The superscript  $-$  as in  $x_0^-$  is the prediction step, whereas the superscript  $+$  is values obtained after the control step. The  $x_0^-$  is a column matrix and it is

$$x_0^- = \begin{bmatrix} z_0^- & \frac{\partial z_0^-}{\partial a} & \frac{\partial z_0^-}{\partial r} \end{bmatrix}_{1 \times 3}^T \quad (9)$$

where  $z_0^-$  is topographic height,  $\partial z_0^- / \partial a$  is the derivative of the height in the azimuth direction, and  $\partial z_0^- / \partial r$  is the derivative of the height in range direction. Averaging coefficients are calculated based on the available (previously solved) neighboring pixels

$$D = \begin{bmatrix} 1/N & 0 & 0 \\ 0 & 1/\sum_{n=1}^N A_N[2, 3n-1] & 0 \\ 0 & 0 & 1/\sum_{n=1}^N A_N[3, 3n] \end{bmatrix}_{3 \times 3} \quad (10)$$

where  $N$  is the number of available neighbors, and  $A_N[i, j]$  is the element located at row  $i$ , column  $j$  of the transition matrix. As seen from (11), the sum of elements in second row and every second column in the  $A_N$  matrix provides the number of neighbors available in azimuth direction. Similarly, the sum of elements in the third row and every third column provides the number of neighbors in range direction

$$A_N = \begin{bmatrix} 1 & \Delta a_1 & \Delta r_1 & 1 & \Delta a_n & \Delta r_n \\ 0 & |\Delta a_1| & 0 & \dots & 0 & |\Delta a_n| & 0 & \dots \\ 0 & 0 & |\Delta r_1| & 0 & 0 & |\Delta r_n| \end{bmatrix}_{3 \times 3N} \quad (11)$$

where  $\Delta a_n$  is the azimuth offset between the  $n$ th neighbor and current pixel, and similarly  $\Delta r_n$  gives the range offset for the  $n$ th neighbor. The information from  $N$  already solved neighbors are given in  $x_N$

$$x_N^+ = \begin{bmatrix} z_1^+ & \Gamma \frac{\partial z_1^+}{\partial a_1} & \Gamma \frac{\partial z_1^+}{\partial r_1} & \dots & z_n^+ & \Gamma \frac{\partial z_n^+}{\partial a_n} & \Gamma \frac{\partial z_n^+}{\partial r_n} & \dots \end{bmatrix}_{1 \times 3N}^T \quad (12)$$

where the first three elements of  $x_N$  row vector holds the topographic height estimate ( $z_1^+$ ) for the first point, the gradient in azimuth direction  $\partial z_1^+ / \partial a_1$ , and in range direction  $\partial z_1^+ / \partial r_1$ .  $\Gamma$  is a phase stability coefficient and can be thought as an average coherence for the stack of input interferograms; we obtained better results, however, with the quality values defined based on the Fisher's Distance defined in (6). Phase stability coefficient using Fisher's Distance can be calculated as

$$\Gamma = 1 - \overline{FD}_0 \quad (13)$$

where  $\overline{FD}_0$  is the normalized Fisher's Distance. Normalization is achieved by dividing  $FD_0$  by the maximum Fisher's Distance calculated in the image to satisfy  $0 \leq \overline{FD}_0 \leq 1$ . The maximum value of Fisher's Distance for interferometric

data is around  $\pi$ , though slightly larger. As in (12), the weighting is applied to the state vector's gradient components directly, instead of multiplying the factors in the relation matrix ( $A_N$ ). After testing both alternatives presented in this paper, we concluded that direct weighting of the state vectors produces better results, because weighting the  $A_N$  matrix also weights the error covariance [60].

The observation vector  $y_M$  consists of real and imaginary components of all available observations as well as phase derivatives in azimuth and range directions. Placing the phase gradients into the observation vector constrains the filter to fit both the phase values and the phase gradients, and removes the requirement for calculating them separately

$$y_M = \begin{bmatrix} \Re(y_1)/|y_1|, \Im(y_1)/|y_1|, \partial \angle \phi_1 / \partial a, \\ \partial \angle \phi_1 / \partial r, \dots, \Re(y_m)/|y_m|, \Im(y_m)/|y_m|, \\ \partial \angle \phi_m / \partial a, \partial \angle \phi_m / \partial r, \dots \end{bmatrix}_{1 \times 4M}^T \quad (14)$$

where  $\Re$  and  $\Im$  are real and imaginary values,  $|\cdot|$  shows absolute value and  $M$  is the number of InSAR observations. The  $\partial \angle \phi_m / \partial a$  is the partial derivative of phase angle in azimuth direction for interferogram  $m$ . Likewise, the  $\partial \angle \phi_m / \partial r$  is the phase derivative in the range direction.

The  $H_M$  converts the linear Kalman filter predictions to nonlinear values for comparison with the observed data

$$H_M(x_0^-) = \begin{bmatrix} \cos\left(\frac{\Delta \phi_1}{\Delta z} z_0^-\right), \sin\left(\frac{\Delta \phi_1}{\Delta z} z_0^-\right), \\ \frac{\Delta \phi_1}{\Delta z} \frac{\partial z_0^-}{\partial a}, \frac{\Delta \phi_1}{\Delta z} \frac{\partial z_0^-}{\partial r}, \dots, \cos\left(\frac{\Delta \phi_m}{\Delta z} z_0^-\right), \\ \sin\left(\frac{\Delta \phi_m}{\Delta z} z_0^-\right), \frac{\Delta \phi_m}{\Delta z} \frac{\partial z_0^-}{\partial a}, \\ \frac{\Delta \phi_m}{\Delta z} \frac{\partial z_0^-}{\partial r}, \dots \end{bmatrix}_{1 \times 4M}^T \quad (15)$$

where  $\Delta \phi_m / \Delta z$  is the height-to-phase conversion factor for interferogram  $m$  as described in (3). It is clear from (8), (14), and (15) that phase derivatives are assumed to be unwrapped, such that  $\partial \angle \phi_m / \partial a = (\Delta \phi_m / \Delta z)(\partial z_0^- / \partial a)$ .

Using the state-space equations given in (7) and (8) we can define the Kalman filter. In the prediction step, the state-space model is used to predict the state vector and the error covariance of the next point based on a previous solution. In DEM generation, the previous solution may indicate any neighboring pixel. Therefore, as in Fig. 1(d), the prediction step condenses information from all available neighbors into a single prediction. In the control step, predictions are compared with the observation vectors and corrections are applied to the state vector. The box diagram for the two steps of operations for the designed Kalman filter is shown in Fig. 1(d).

In the prediction step, state vectors from each neighbor are averaged, assuming equal weighting for all directions. The validity of this operation and the assumptions behind it are given in the appendix. Given the nature of different characteristics between azimuth and range directions, a resolution-related weighting can be applied. For this research, we use square pixel dimensions and weighting is, thus assumed equal. Another weighting approach could be based on the distance

between current and neighboring pixels, and still a third approach could be implemented based on a measure of the phase stability (e.g., coherence) of neighboring pixels. We use a neighborhood of  $3 \times 3$  and weight the state vector gradients based on the phase stability of the point while giving the corner pixels equal weight as others (in terms of distance) for the sake of simplicity. EKF combines the information from already-solved neighboring pixels in the prediction step given as

$$x_0^- = DA_N x_N^+ \quad (16)$$

where  $x_0^-$  is the current state,  $D$  is the  $3 \times 3$  averaging coefficient,  $A_N$  is the  $3 \times 3N$  relation matrix,  $x_N$  is the  $3N \times 1$  matrix of neighbor states. The state prediction equation is essentially the same as (7) besides the noise term. The error covariance is predicted using

$$P_0^- = DA_N P_N^+ A_N^T D^T + Q_0 \quad (17)$$

$$P_N^+ = \begin{bmatrix} P_1^+ & 0 & 0 & 0 \\ 0 & \ddots & 0 & 0 \\ 0 & 0 & P_n^+ & 0 \\ 0 & 0 & 0 & \ddots \end{bmatrix}_{3N \times 3N} \quad (18)$$

where  $P_0^-$  is  $3 \times 3$  error covariance, and  $Q_0$  is the  $3 \times 3$  process noise covariance. Tuning an EKF can be painstaking, and calculating the process noise covariance ( $Q$ ) can be particularly difficult as the estimated process cannot be directly observed [54], [60]. As in (8), observations ( $y$ ) are related to the state vector ( $x$ ) through a nonlinear function  $H$ . Further complicating the tuning, the linearizations in the EKF are known to underestimate the calculated error [60]. The process in this case is the height of a point that is only observed by the synthetic aperture radar in wrapped form, under certain assumptions and with a certain noise level. For some models, a constant process covariance matrix can be used; for InSAR measurements, however, the process covariance matrix needs to be updated at each point because the phase and interferogram quality change constantly. One way to estimate the process noise might be to calculate the average height variance expected from the interferometric data

$$\sigma_z^2 = \frac{1}{M} \sum_{m=0}^M \sigma_{z_m}^2 = \frac{1}{M} \sum_{m=0}^M \left( \sigma_{\phi_m} / \frac{\Delta \phi_m}{\Delta z} \right)^2 \quad (19)$$

where the  $\sigma_z^2$  is the expected height variance,  $\sigma_{z_m}^2$  is the variance of interferogram  $m$  in meters,  $\sigma_{\phi_m}$  is the standard deviation of phase for interferogram  $m$ , and the  $\Delta \phi_m / \Delta z$  is the height-to-phase conversion factor given in (3). The variance (or standard deviation) of phase values for each interferogram can be calculated from coherence [66], phase derivative variance [67], [68], or Fisher's Distance [65]. We determined through experimentation that overestimating the process noise covariance indeed improves the results, probably because of the filter's noise characteristics. In the proposed method, the process noise covariance is calculated based on the Fisher's Distance and the minimum absolute height-to-phase conversion factor for all interferograms. The process noise covariance

matrix is then constructed after Krämer [45]

$$Q_0 = \begin{bmatrix} 0 & 0 & 0 \\ 0 & \overline{FD}_0 / \min(|\frac{\Delta \phi_M}{\Delta z}|)^2 & 0 \\ 0 & 0 & \overline{FD}_0 / \min(|\frac{\Delta \phi_M}{\Delta z}|)^2 \end{bmatrix}_{3 \times 3} \quad (20)$$

where  $Q_0$  is the process noise covariance,  $\overline{FD}_0$  is the average Fisher's Distance for the current point,  $\min(|\cdot|)$  is the minimum of the absolute value, and  $\Delta \phi_M / \Delta z$  is a vector of height-to-phase conversion factors for the current point in  $M$  interferograms. Better estimation of the process noise covariance matrix ( $Q_0$ ) might be a possible future improvement to unwrapping interferograms with EKFs.

When available, an existing DEM can be provided as an input to the prediction step, which can then be combined with the filter estimates to initialize the next state as shown

$$x_0^{-,init} = \Gamma x_0^- + (1 - \Gamma) x_0^{init} \quad (21)$$

where  $x_0^{-,init}$  is the new estimate with initialization (DEM),  $x_0^-$  is prediction based on neighboring states,  $\Gamma$  is the phase stability coefficient defined in (13), and  $x_0^{init}$  is the initialization state vector calculated from the existing DEM. Incoherent areas separating coherent regions (e.g., Istanbul Bosphorus, Section IV-B.) pose a specific difficulty for path-following algorithms. Because the phase of neighboring pixels in incoherent areas is not correlated, results of unwrapping over such areas become invalid. (21) shows that for completely incoherent areas (e.g., over water,  $\Gamma \approx 0$ ) the Kalman filter prediction is highly dependent on the given reference DEM. In addition, as in (21), the initialization is not only used for the topography but is also used to initialize the gradients. Therefore, even though subtracting the known topography from interferograms would simplify the unwrapping operation by reducing fringe density, it can lead to degraded filter performance over incoherent areas.

In the control step of the filter, the predicted state values ( $x$ ) are compared with the observation ( $y$ ) values. The governing equations for this step are similar to any parallel EKF

$$x_0^+ = x_0^- + K_M r_M \quad (22)$$

$$P_0^+ = P_0^- - K_M C_M P_0^- \quad (23)$$

where  $x_0^+$  is the state estimate after the control step,  $x_0^-$  is the state estimate from the prediction step,  $K_M$  is the Kalman filter gains calculated for  $M$  interferograms, and  $r_M$  is the residuals for  $M$  phase observations. The  $P_0^+$  is the error covariance after the control step,  $P_0^-$  is the error covariance from the prediction step, and  $C_M$  is the linearization of the nonlinear relation operation ( $H_M$ ). Further information on  $K_M$ ,  $C_M$ , and  $r_M$  are given between (24) and (29).

Kalman filter gain ( $K_M$ ) is calculated for each point in each interferogram based on the ratio of the error covariance ( $P$ ) to the sum of both error and measurement noise covariances ( $P$  and  $R$ ). Error covariance matrix ( $P_0^+$ ) is linearized by  $C_M P_0^+ C_M^T$

$$K_M = P_0^+ C_M^T [C_M P_0^+ C_M^T + R_M]^{-1} \quad (24)$$

where  $R_M$  is the measurement noise covariance and superscript  $-1$  is the matrix inversion. The linearization matrix  $C_M$

is defined as the differential of the nonlinear relation matrix ( $H_M$ ). The linearization matrix and measurement covariance matrix are

$$C_M = [C_1 \cdots C_m \cdots]_{4M \times 3} \quad (25)$$

$$C_m = \begin{bmatrix} -\frac{\Delta\phi_m}{\Delta z} \sin(\frac{\Delta\phi_m}{\Delta z} z_0) & \frac{\Delta\phi_m}{\Delta z} \cos(\frac{\Delta\phi_m}{\Delta z} z_0) & 0 & 0 \\ 0 & 0 & \frac{\Delta\phi_m}{\Delta z} & 0 \\ 0 & 0 & 0 & \frac{\Delta\phi_m}{\Delta z} \end{bmatrix}_{4 \times 3} \quad (26)$$

$$R_M = \text{diag}[R_1 \cdots R_m \cdots]_{4M \times 4M} \quad (27)$$

$$R_m = [\sigma_{z_m}^2 \quad \sigma_{z_m}^2 \quad 2\sigma_{z_m}^2 \quad 2\sigma_{z_m}^2]_{1 \times 4} \quad (28)$$

where  $C_M$  is a  $4M \times 3$  matrix consisting of  $M$   $C_m$  matrices,  $R_M$  is the measurement covariance matrix. *diag* operator constructs a diagonal matrix, and  $\sigma_{z_m}$  is the estimated height variance.

The residual matrix ( $r_M$ ) is obtained by comparing predicted state ( $x_0^-$ ) with the interferometric phase observations ( $y_M$ )

$$r_M = y_M - H_M(x_0^-) \quad (29)$$

where  $y_M$  is the observation matrix in (14) and  $H_M$  is the nonlinear relation operation in (15). As in (24), the error covariance matrix ( $P_0$ ) is multiplied by  $C_M$  to calculate Kalman gain  $K_M$ . The height-to-phase conversion factor  $\Delta\phi/\Delta z$  is directly proportional to perpendicular baseline. Multiplication of  $\Delta\phi/\Delta z$  with  $P_0$  has the adverse effect of scaling the error variance in favor of the small baseline interferograms that are less sensitive to the topography. Therefore, we modify (14), (15), and (25) such that all terms are divided by  $\Delta\phi/\Delta z$ . The control step of the developed EKF is iterative, similar to locally iterative EKF, to better estimate the state in high nonlinearity [69]. The maximum number of iterations is set by user input (we used 10), where the improvements in the state vector are also compared against a threshold to avoid unnecessary iterations.

#### IV. APPLICATIONS

Three separate data sets are used to test three important aspects of our method. The first is a synthetic data set, for verifying that the underlying assumptions of the algorithm are correct and that the filter can unwrap multiple interferograms simultaneously to obtain a combined topography map. The second data set consists of C-band Envisat advanced synthetic aperture radar (ASAR) imagery acquired over Istanbul, Turkey. This data set is appropriate for testing the algorithm's stability on coherent patches separated by low-coherence areas, because of water bodies like the Bosphorus. The final data set is X-band TerraSAR-X strip-mode data acquired over Juarez-El Paso. The TerraSAR-X data provides the opportunity to test the filter's topography improvement functionality, as an independent, high-resolution DEM for the area is available. In addition, the Envisat and TerraSAR-X data allow for a comparison between EKF's results and those of the conventional DEM generation method, namely a weighted average of individually unwrapped interferograms using the SNAPHU, as well as the results from 3-D maximum likelihood algorithm

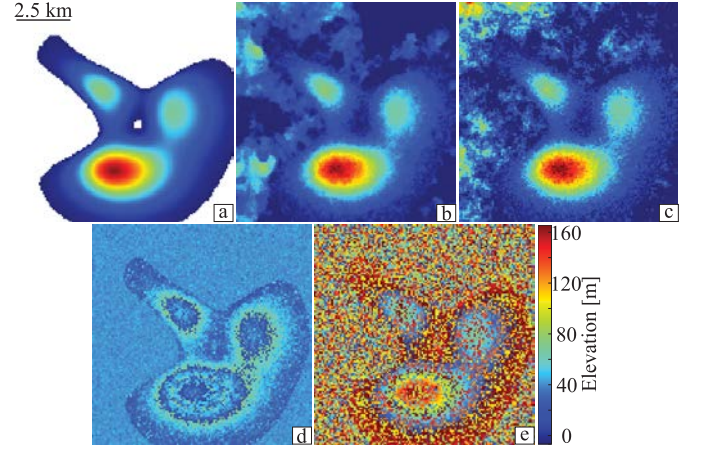


Fig. 2. (a) Radar-coded synthetic DEM based on smooth surface defined using (30). Areas below 1 m are assigned as water bodies, and are masked with white color. In addition large surrounding water body,  $3 \times 5$  pixels large lake is simulated at low point of simulated island. (b) Height values calculated by EKF. (c) Height values calculated by SNAPHU. (d) Height values calculated by 3-DMLE with normal distribution. (e) Height values calculated by 3-DMLE with uniform distribution.

(3-DMLE) [6], [70]–[72], [13]. Even though 3-DMLE algorithm is used for DEM reconstruction from SAR data in previous studies, it is designed to work with single pass interferograms and does not handle well the noise sources related to multiple pass interferometry.

##### A. Synthetic Data

The first test case for our new algorithm is generated based on a  $128 \times 128$  pixels synthetic DEM, calculated as a sum of several shifted Gaussian functions defining a smooth surface. To test the behavior of the filter in low-coherence areas and judge the effectiveness of the quality-based unwrapping paths, areas below 1 m are assigned as water bodies, with no coherence. The synthetic DEM was calculated using [73]

$$\begin{aligned} \text{DEM}(x, y) = & 20 \times (3 \times (1 - x)^2 \times e^{-x^2 - (y+1)^2} \\ & - 10 \times (x/5 - x^3 - y^5) \times e^{-x^2 - y^2} \\ & - 1/3 \times e^{-(x+1)^2 - y^2}) \end{aligned} \quad (30)$$

where  $x$  and  $y$  are 2-D space, and  $e$  is Euler's number ( $e = 2.7183$ ). The visualization of the resulting synthetic DEM with the underwater areas marked as 0 m are shown in Fig. 2(a).

Two interferograms are generated using European Remote Sensing satellite (ERS)-like parameters: 0.05666 m wavelength, 19 degrees look angle to the first pixel, 830 km range to the first pixel, and 80-m pixel resolution. The interferograms are simulated for baselines of 100 m and 150 m. Noise levels are calculated based only on the signal strength derived from the DEM slope, and other noise sources such as atmosphere are neglected. The resulting interferograms and coherence values are shown in Fig. 3.

The unwrapping operation commenced at the highest-quality pixel in the data set as a reference point, with the assumption that the height of the reference pixel is zero. The actual elevation of this point in the synthetic DEM is 16.52 m.

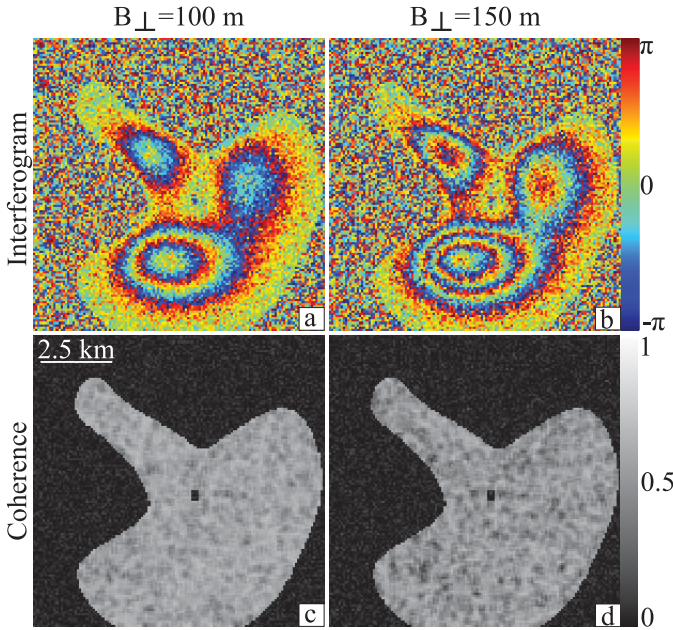


Fig. 3. Synthetic interferograms generated using DEM shown in Fig. 2(a). (a) Phase values of synthetic interferogram with 100-m baseline. (b) Phase values of synthetic interferogram with 150-m baseline. (c) Coherence values for 100-m interferogram. (d) Coherence values for 150-m interferogram.

The DEM calculated by EKF is shown in Fig. 2(b). EKF and SNAPHU results for the synthetic data are very similar over the island, though EKF result is slightly smoother [Fig. 2(b) and (c)]. The 3-DMLE algorithm requires some information about the entire imaged area, and as a coarse resolution DEM is not made available to EKF and SNAPHU algorithms, two different initializations are tested to generate the 3-DMLE results: first assumption uses the mean and standard deviation of the DEM to generate a normal distribution [Fig. 2(d)], whereas the second assumption uses the minimum and maximum heights defining a uniform distribution [Fig. 2(e)]. The uniform distribution essentially uses only the information available from the synthetic interferograms, whereas the Gaussian distribution modifies the joint probability. Therefore, the 3-DMLE algorithm with Gaussian distribution generates values near the mean height (29.10 m) while the 3-DMLE algorithm with uniform distribution generates values within the entire range.

### B. Envisat Data

The Envisat data consists of six interferograms generated from ascending track 429, frame 27, with a look angle of  $20^\circ$ , acquired between October 2003 and August 2009. Previous studies show that there is deformation in some areas of Istanbul, which will add additional noise to the topographic signal measured over the six-year period [74], [75]. To suppress the deformation signal, all selected interferograms have short temporal baselines of 35 or 70 days. Temporal and perpendicular baseline information for the interferograms are shown in Fig. 4. To ensure that the interferograms are stacked correctly, all of the images are resampled according to a common resampling master. The image acquired on 21

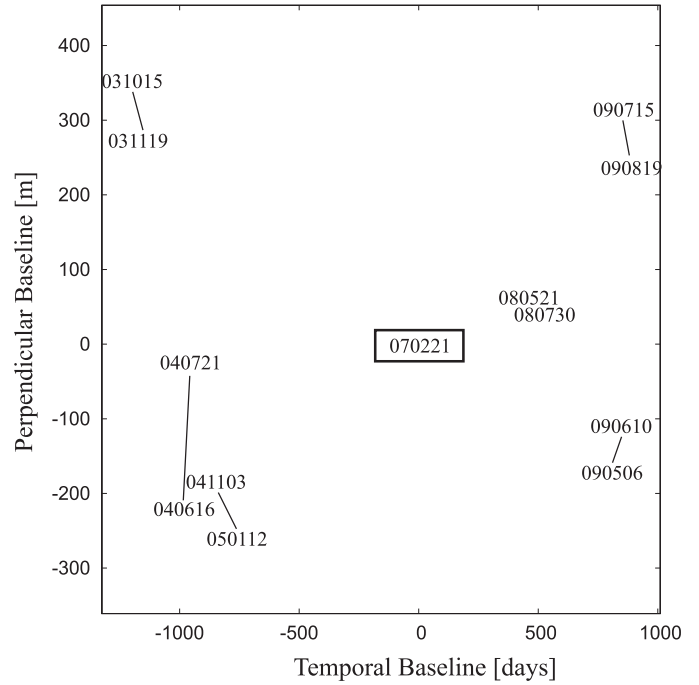


Fig. 4. Plot of temporal versus perpendicular baselines for Envisat data over Istanbul. Labels indicate dates of scenes in yymmdd format. Center of labels mark their location on plot. Scene acquired on 070221 is resampling master, indicated by box. Lines connect pairs of interferograms (line between 080521 and 080730 is not shown).

February 2007 was selected as the resampling master because it minimizes the total temporal and spatial baseline separations for interferograms.

The phase and coherence of the interferograms are shown in Fig. 5(a) and (b). Interferograms are about  $80 \times 80$  km and are sorted left-to-right in the order of perpendicular separation (absolute perpendicular baseline). Coherence is generally high over urban areas, however the northern part of the land cover is heavily vegetated, resulting in low coherence. The minimum perpendicular baseline to obtain a DEM accuracy of 1 m is 60 m, to map a total height difference of 400 m with an orbital accuracy of 15 cm RMS (4). Therefore, the interferogram with the shortest perpendicular baseline, 080521–080730, is affected by a residual plane even though Envisat DORIS precise orbits state vectors (DOR\_VOR\_AX) are used [76], [77].

During small scale tests, filter stability emerged as an area of concern, where certain patches could have large phase jumps from their surroundings. To eliminate the divergence issue of the filter, SRTM 3 arcsec data were used to initialize the filter. As in Section III, when available the initial solution is used to calculate initial values for the EKF state vector. The initial SRTM 3 arcsec DEM, and EKF solution are shown in Fig. 6(a) and (b). There is good overall agreement between the SRTM DEM and the topography obtained by EKF. In Section V, we show that EKF generates some significant improvements.

Conventional DEM generation relies on the unwrapping of individual interferograms [70]. The SNAPHU unwrapping algorithm [71], [72], [78], [79] was used to individually unwrap the interferograms. In an effort to equalize the input

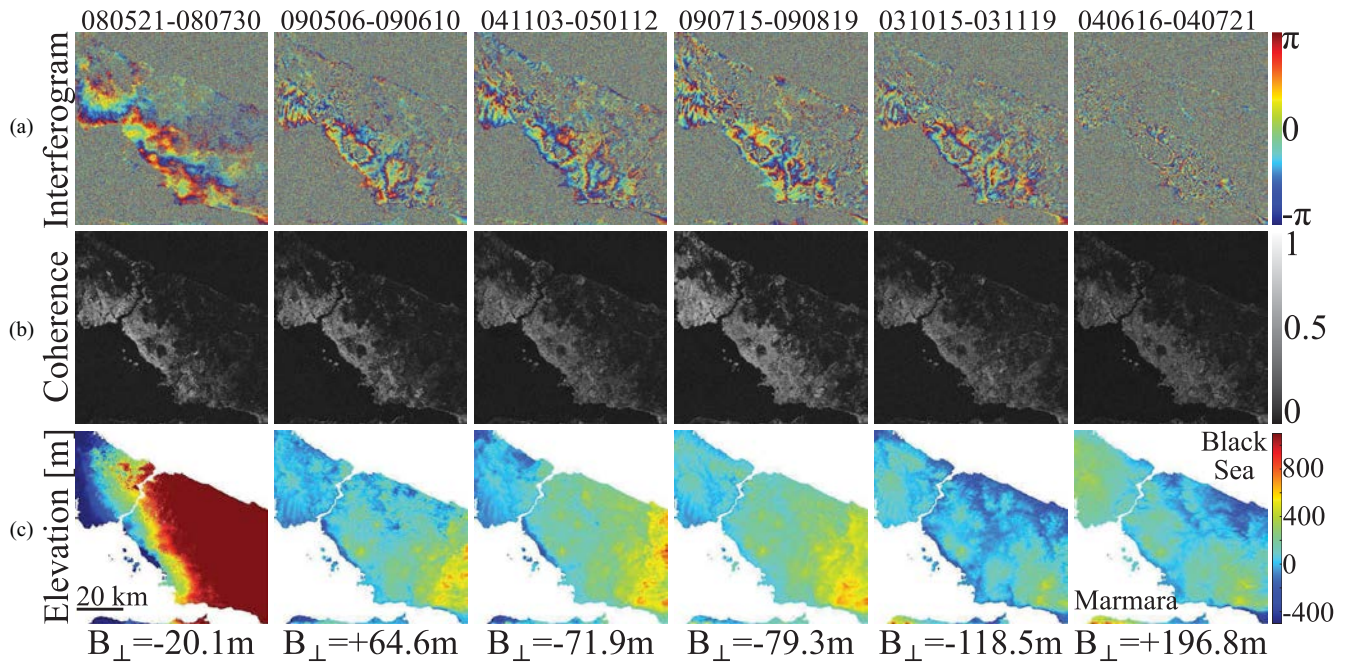


Fig. 5. (a) Interferograms generated using Envisat ASAR data over Istanbul, Turkey, sorted in order of increasing absolute baseline. As baseline separation increases more fringes become visible. Because of increased fringe rate 040616–040721 interferogram looks incoherent. (b) Coherence values for the interferograms. Coherence image of 040616–040721 indicate similar quality to others. (c) Topographic heights obtained using conventional methods from InSAR data. Unwrapping result for 080521–080730 interferogram is affected by large ramp, probably because of residual plane in wrapped interferogram.

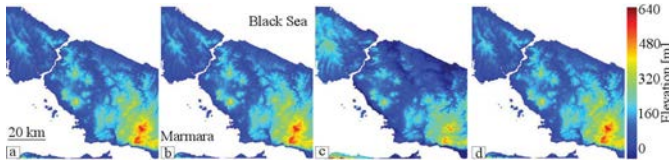


Fig. 6. (a) SRTM 3 arcsec DEM resampled to radar coordinates. (b) Topography obtained by EKF. (c) Topography obtained by weighted average of SNAPHU results. (d) Topography obtained by 3-DMLE.

for both SNAPHU and EKF, the topographic phase signal is calculated for each interferogram and specified as the coarse unwrapped-phase estimate, whereas coherence is given to specify correlation. Unwrapped phase values are then processed further in DORIS interferometry software to calculate height values [80]. The resulting height values are further adjusted such that the reference point of EKF DEM value is equal to the height value in SRTM DEM. The final height values are shown in Fig. 5(c).

Weighted averaging of five out of the six interferograms provided a comparable DEM using SNAPHU. The 080521–080730 interferogram is omitted from the weighted average because of the large ramp in the unwrapped result. The topographic heights calculated from the interferograms are averaged using ML Gaussian estimation [10], [41]

$$z_{ML} = \frac{\sum_{m=0}^M z_m / \sigma_{z_m}^2}{\sum_{m=0}^M 1 / \sigma_{z_m}^2} \quad (31)$$

where  $z_{ML}$  is the ML height estimate,  $M$  is the number of interferograms,  $z_m$  is the topographic height derived from interferogram  $m$ , and  $\sigma_{z_m}^2$  is the variance of height measurement for interferogram  $m$  as defined in (19). The

resulting DEM closely matches the SRTM 3 arcsec DEM [Fig. 6(c)].

Results from another 3-D algorithm, namely the 3-DMLE are generated for comparison [13]. The 3-DMLE algorithm is able to unwrap and fuse InSAR observations at the same time, similar to EKF. In addition, it can also be initialized using an existing DEM. The 3-DMLE algorithm can also work in a geodetic coordinate system, utilizing geocoded interferograms, however as the results presented in this paper are in radar coordinates, the processing is kept in radar coordinates. The 3-DMLE algorithm requires the interferograms to have a common reference point, and all orbital fringes must be removed from the data. Therefore, similar to the analysis with SNAPHU, the 080521–080730 interferogram is omitted for 3-DMLE analysis. The 3-DMLE algorithm works by finding the height estimate with the highest probability in a given search space. For this analysis, the search space is set to cover a range of six standard deviations around the observed height value of the input DEM. As in EKF, the standard deviation of SRTM 3arcsec DEM for 3-DMLE is considered as 10 m, thereby creating a 60 m wide search-space around the observed value, at a resolution of 0.1 m.  $2\pi$  aliased probability distributions for each InSAR observation are mapped to this domain depending on the observed phase and coherence values. The results of the 3-DMLE algorithm obtained over Istanbul are shown in Fig. 6(d).

### C. TerraSAR-X Data

The X-band, repeat-pass interferometric data collected by TerraSAR-X has some differences compared with the C-band Envisat data. The 11-day repeat cycle of TerraSAR-X and its

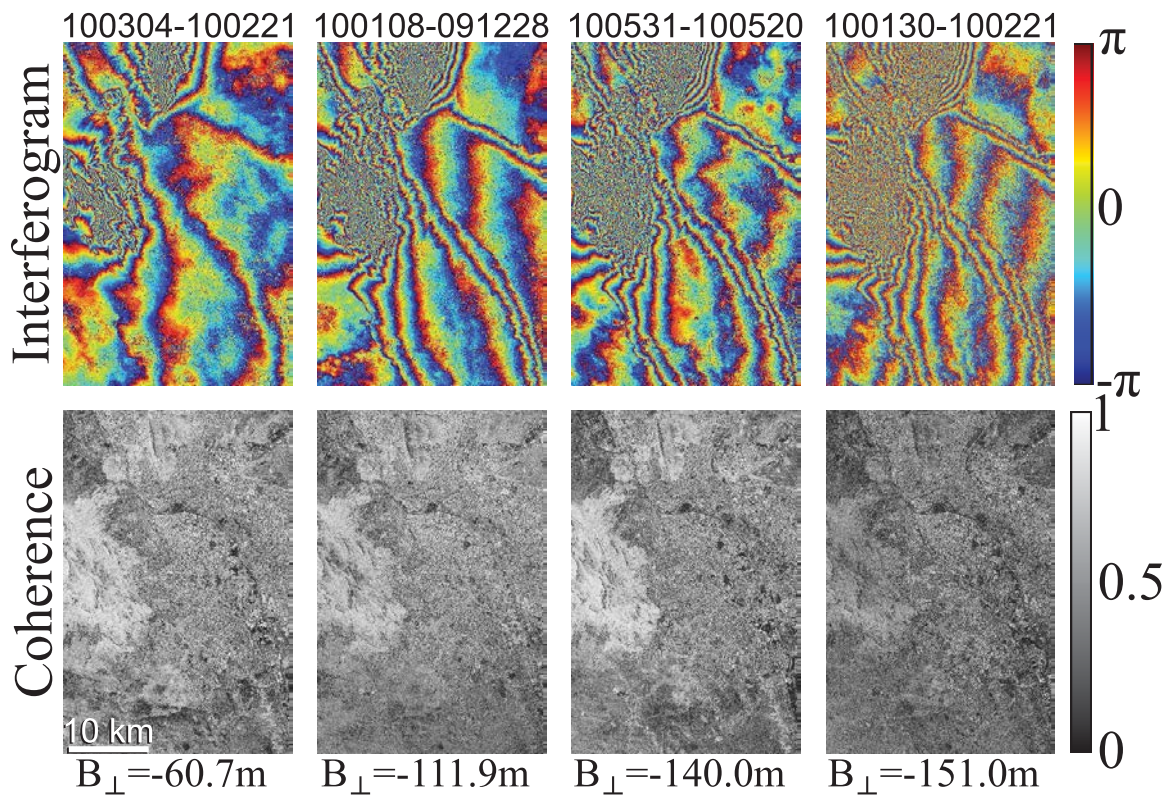


Fig. 7. Interferograms generated using TerraSAR-X data over Juarez-El Paso, sorted in order of increasing absolute baseline length. As baseline separation increases more fringes become visible. 100130–100221 interferogram has temporal baseline of 22 days, resulting in lower coherence compared with interferograms with 11 days baseline.

high-spatial resolution result in highly coherent interferograms compared with Envisat interferograms with 35-day repeat interval. High coherence values are also observed in wetlands using TerraSAR-X imagery [81]. The TerraSAR-X data were collected over Juarez-El Paso between 28 December 2009 and 25 July 2010 on ascending track in strip-map mode with a look angle of  $26.4^\circ$ , with both azimuth and range pixel spacing of  $\sim 1.8$  m. For this analysis, we multilooked the interferograms to  $\sim 10 \times 10$  m square pixels. Among the 15 available scenes, we selected four interferograms to test the generation of a higher resolution DEM by combining a coarse resolution DEM with higher resolution interferograms.

The selection criteria for the four pairs out of 15 scenes is based on the orbital error and critical baseline. TerraSAR-X orbits are thought to be precise to better than 3 cm rms based on laser ranging measurements and the 3-D absolute orbit accuracy is thought to be better than 10 cm [82]. If we assume an orbital accuracy of 5 cm, and the requirement of a 1 m baseline, mapping a height difference of 800 m will require a minimum perpendicular separation of:  $(0.05/1) \times 800 = 40$  m. The critical perpendicular baseline for TerraSAR-X, with the slope calculated using SRTM 3 arcsec DEM, is over 4 km. However, to simplify the unwrapping procedure over mountainous terrain, we selected pairs with less than 200 m perpendicular baseline. Table I shows the baseline information for the pairs used in this analysis and Fig. 7 shows the phase and coherence values of selected interferograms. Unlike the Envisat data set, TerraSAR-X interferograms are not

TABLE I  
BASELINE INFORMATION FOR TERRA SAR-X INTERFEROGRAMS

Master-Slave <sup>1</sup> [dates]	Temp. <sup>2</sup> Baseline [days]	Perp. <sup>3</sup> Baseline [m]	Par. <sup>4</sup> Baseline [m]
100304-100221	-11	-60.7	-15.1
100108-091228	-11	-111.9	-39.6
100531-100520	-11	-140.0	-74.3
100130-100221	22	-151.0	-78.1

<sup>1</sup> Master and slave dates are in yymmdd format.

<sup>2</sup> Temporal

<sup>3</sup> Perpendicular

<sup>4</sup> Parallel

coregistered to a single master image. The precise science orbits provided by DLR have a registration accuracy of 1 m [83]. This high level of orbit accuracy results in a negligible 1/10 pixel coregistration error. Therefore, individual interferograms are cropped to the same area based on coordinates on the reference ellipsoid, instead of coregistering all images to a single master.

The interferograms and coherence values are shown in Fig. 7. For the Juarez-El Paso test site three DEMs are available: SRTM 3 arcsec, SRTM 1 arcsec, and NED 1/9 arcsec DEM [84] [Fig. 8(a)–(c)].

Fig. 8(a) suggests that the SRTM 3 arcsec DEM actually provides more detail than the SRTM 1 arcsec DEM over the mountainous area to the west (Cerro Bola Mountains); the

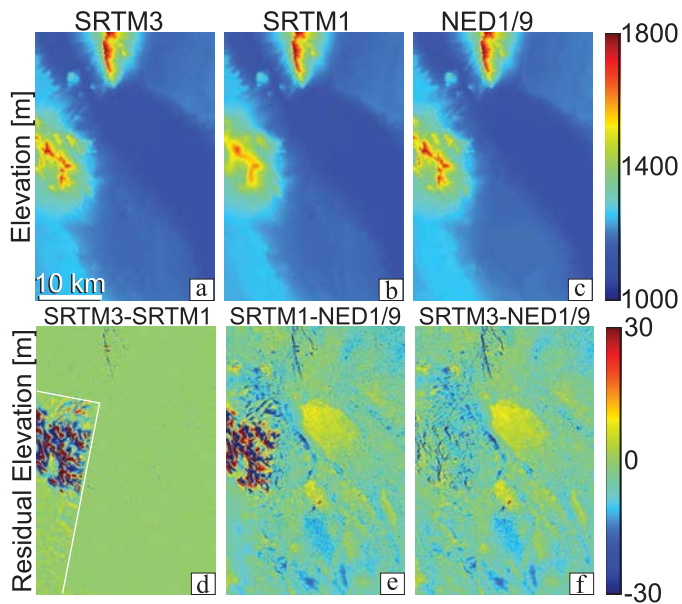


Fig. 8. Available DEMs and their differences for Juarez-El Paso test site. DEMs are resampled in radar coordinates to same resolution as multilooked interferogram. (a) SRTM 3 arcsec DEM. (b) SRTM 1 arcsec DEM. (c) NED 1/9 arcsec DEM. (d) SRTM 1 arcsec DEM subtracted from SRTM 3 arcsec. (e) SRTM 1 arcsec subtracted from NED 1/9 arcsec. (f) SRTM 3 arcsec subtracted from NED 1/9 arcsec. Area outlined in white in Fig. 8(d) indicates problematic area.

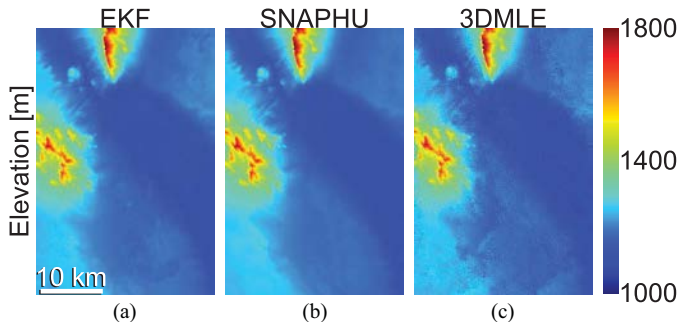


Fig. 9. DEMs generated over Juarez-El Paso. (a) Topography obtained by EKF. (b) Topography obtained by weighted average of SNAPHU results. (c) Topography obtained by 3-DMLE.

reason for this is unclear. Considering the difference between SRTM 1 arcsec and SRTM 3 arcsec DEMs reveals that the data are identical for most of the area except for the Cerro Bola mountains. The residuals between DEMs are shown in Fig. 8(d)–(f). Because of the smaller residuals between SRTM 3 arcsec and NED 1/9 arcsec DEMs, SRTM 3 arcsec data set is used as an initial solution for EKF and SNAPHU. The NED 1/9 arcsec DEM is used as a benchmark. EKF, SNAPHU and 3-DMLE results are obtained as described in Section IV-B (Fig. 9).

## V. DISCUSSION

Over the past decade, the SRTM provided a DEM at resolutions of 3 and 1 arcsec for many parts of the world [41], [85]. The advanced spaceborne thermal emission and reflection radiometer (ASTER) global DEM mission provided worldwide coverage at a resolution of 1 arcsec, however ASTER GDEM

is adversely affected by processing artifacts in the mosaicking step [86], [87]. The TanDEM-X mission will soon be able to generate DEMs with global coverage at resolutions at or above 1/3 arcsec [13], [88]. Although availability of high resolution DEMs increases over time, there is still a need to solve for the topographic signal in InSAR data, especially when high resolution DEMs are not available, bare-earth DEMs are not suitable for the application, or if the landscape has changed since the DEM was generated, e.g., active volcanoes.

Comparison of DEMs can be done by analyzing residuals and misfits. Residuals are obtained by differencing a given DEM from a benchmark DEM or differencing the topographic signal of the obtained DEM from the interferogram. Residuals can be negative or positive, and are not weighted. Misfit, on the other hand, is weighted by the expected error, and is only a scalar measure of agreement between two observations. Misfit can be calculated as

$$\chi = \sqrt{\left\langle \frac{[\hat{z} - z]^2}{\sigma_z^2} \right\rangle} \quad (32)$$

where  $\chi$  is the misfit,  $\langle \cdot \rangle$  is the average,  $\hat{z}$  is the solution,  $z$  is the known DEM, and  $\sigma_z^2$  is the expected variance of height values defined in (19). Because the units for the numerator and denominator in (32) are the same, the reported misfit values are unitless, and are ratios of obtained and expected variance at each point. The following sections discuss misfits corresponding to synthetic, Envisat and TerraSAR-X data sets.

### A. Synthetic Data

In path-following unwrapping, large errors accumulated in an area can indicate error propagation issues. Additional trends or divergence in the results would indicate errors in the state-space model. Misfit values for the synthetic data are shown in Fig. 10.

Misfit maps in Fig. 10 show that the EKF and SNAPHU solutions are accurate over the coherent area. The small ( $3 \times 5$ ) incoherent area in the middle of the test DEM does not show a large misfit, indicating that the EKF is able to deal with small noisy patches surrounded by high-quality points. The 3-DMLE results have higher levels of misfits with both the Gaussian and uniform distributions. The location of the larger misfits change however, from higher altitudes in Gaussian solution to lower altitudes in uniform distribution. This is related to the joint height ambiguity of the two interferograms. The two synthetic interferograms have perpendicular baselines of 100 and 150 m, corresponding to 76.66 and 51.22 m height ambiguities. Therefore, the joint height ambiguity is at 153.65 m. As the maximum topography in this example is around 165 m, the height values are wrapped and 3-DMLE cannot solve the ambiguity. The phase ambiguity in the 3-DMLE results is visible in Fig. 10(c) and (d), where the misfit changes rapidly from low ( $< 1$ ) to high ( $> 3$ ). Even though the joint ambiguity is 153.65 m, there will be phase discontinuities of smaller intervals because of random gaussian geometric decorrelation. For a coherence value of 0.5, there can be a noise of up to 16 and 11 m,

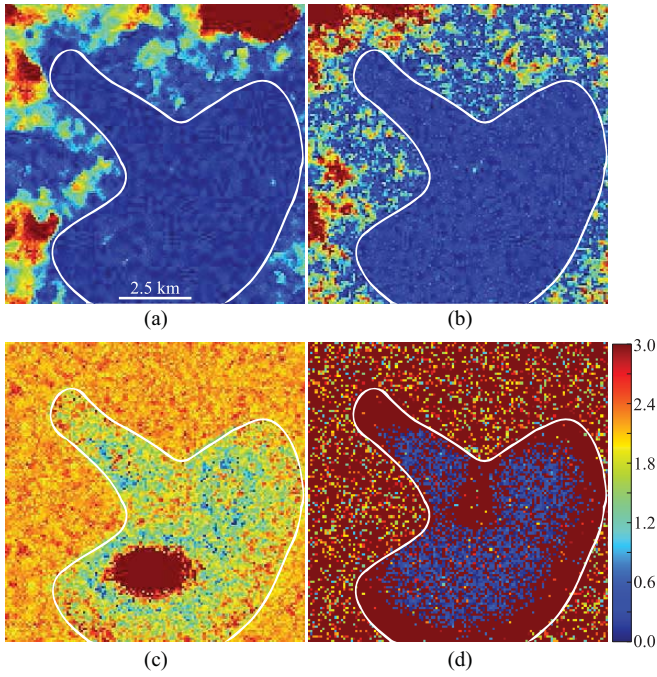


Fig. 10. Misfits for the synthetic DEM. Color-scale is adjusted to show errors in coherent area (inside white curve). (a) EKF result over theoretical water area (outside white curve) diverges quickly as model does not fit to noise. (b) SNAPHU result has similar misfit to EKF. (c) Misfit for 3-DMLE with Gaussian assumption is uniform over low-coherence area, and has large misfit at high altitudes. (d) 3-DMLE with uniform assumption results in large misfits at low altitudes.

respectively, for  $B_{\perp} = 100$  m and  $B_{\perp} = 150$  m baseline interferograms. For example in the uniform approach, the 3-DMLE result has a solution domain between 0 and 165 m, and the ambiguous probability functions of each interferogram repeats at 76.66 and 51.22 m intervals. Therefore, there are about two ( $165/76.66$ ) and three ( $165/51.22$ ) peaks for the respective interferograms. Different additive noise in each interferogram can move the highest probability peak between the two peaks of the 100 m interferogram. This unstable behavior of 3-DMLE with a small number of interferograms is also observed in [13].

Different smoothnesses of EKF, SNAPHU, and 3-DMLE solutions to the synthetic data indicate different error suppression characteristics. For example, the smoother EKF results might be averaging out errors to larger areas, whereas the 3-DMLE solution may result in single pixels with large errors. This behavior can be analyzed by looking at the residuals. Fig. 11 shows the residuals from interferograms, after removing the topographic signal calculated from estimated topography. If the methods estimated the topography correctly, then no large residual signal should be apparent in the resulting image. Lack of fringes in Fig. 11 for EKF and SNAPHU results indicate that both methods indeed solved the topography correctly. The 3-DMLE-Gaussian residual show the ambiguity reversals in color change from blue to red. The 3-DMLE-Uniform method does not show large residuals for the  $B_{\perp} = 150$  m interferogram but shows large residuals for the  $B_{\perp} = 100$  m interferogram.

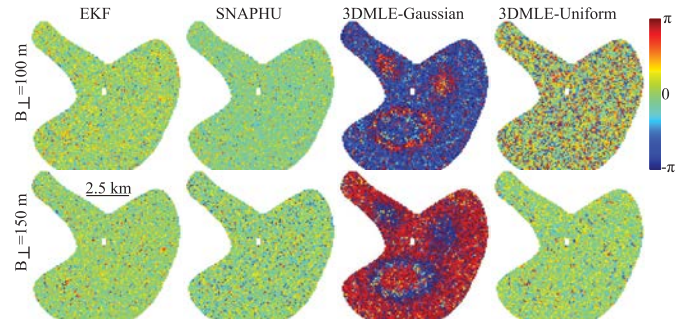


Fig. 11. Residuals for 100 and 150 m synthetic interferograms calculated by removing topographic signal based on EKF, SNAPHU, and 3-DMLE solutions. Large residuals for 3-DMLE.

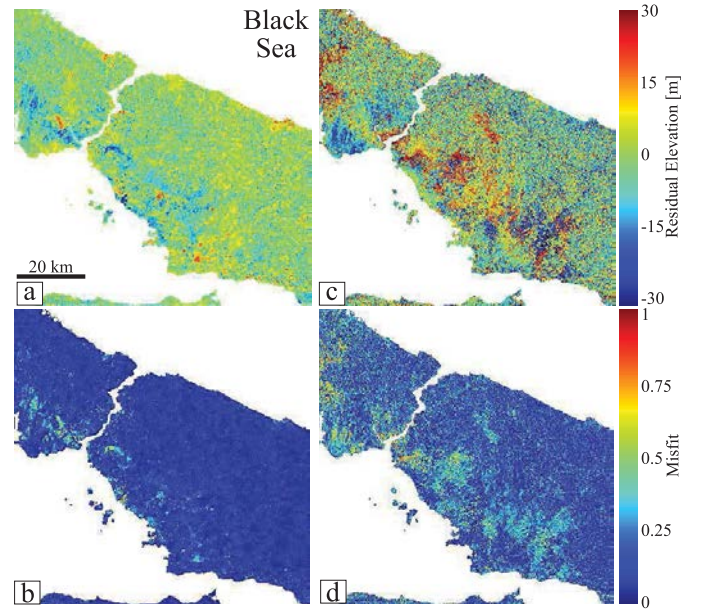


Fig. 12. Residual and misfit for EKF and 3-DMLE on Envisat data set. (a) Differences between EKF DEM and SRTM DEM. (b) Misfit for EKF DEM calculated based on expected error. (c) Differences between 3-DMLE DEM and SRTM DEM. (d) Misfit for 3-DMLE DEM.

### B. Envisat Data

The residuals for the Istanbul-Envisat data confirm that the Kalman filter updates the topographic information where coherent interferometric observations are available, mostly in the coastal areas and especially along the southern coastline. The differences between the SRTM DEM and calculated topography are generally below  $\pm 12$  m, close to the vertical accuracy of SRTM 3 arcsec data [89], [90]. There are some areas with larger differences. The expected disagreement between the obtained DEM and the SRTM DEM can be calculated as  $\sqrt{\sigma_{\text{SRTM}}^2 + \sigma_z^2}$ . We consider the  $\sigma_{\text{SRTM}}$  as  $\pm 10$  m and the  $\sigma_z$  is again the expected variance of height values calculated based on the mean expected phase noise in the interferograms and height-to-phase conversion factor. The differences between the SRTM 3 arcsec DEM and the calculated DEM is shown in Fig. 12(a) and (b) along with the misfit calculated according to (32).

The residuals for the SNAPHU DEM have an east-west trend. This trend is calculated and subsequently removed by

fitting a 2-D first-order polynomial to the residual. Even after detrending, the residuals for the SNAPHU DEM are larger than for those of the DEM obtained by Kalman filtering. The areas with large misfit values ( $> 1.0$ ) are likely because of unwrapping errors. Fig. 13 shows the residuals, detrended residuals, and misfit values for the detrended residuals of SNAPHU solution. The residual and misfit calculated from 3-DMLE algorithm are shown in Fig. 12(c) and (d). Speckle-like characteristics of the residuals in Fig. 12(c) (i.e., changes in residuals from  $-30$  to  $+30$  in neighboring pixels) in comparison with EKF results [Fig. 12(a)] indicate better noise suppression for EKF.

By comparing the misfits shown in Figs. 12(b) and 13(c) it is evident that the Kalman filter was able to combine information from the SRTM DEM and Envisat interferograms without adversely affecting the quality of the final product. The difference in the misfit values are likely because of algorithmic differences between the SNAPHU and EKF. First, SNAPHU unwraps one interferogram at a time, whereas EKF solves all available interferograms at the same time. Second, SNAPHU unwraps by only adding or subtracting  $2\pi$  to the data, whereas EKF filters out the noise. Third, even though both SNAPHU and EKF were initialized with the SRTM 3 arcsec DEM, SNAPHU returns a single unwrapped interferogram while EKF returns a DEM improved by the data in all interferograms. Because of these differences, we could not use the interferogram 080521–080730 in the SNAPHU solution, which had an orbital plane. Looking at the residuals between the SNAPHU-unwrapped interferograms and the input interferograms would return zero residuals, because SNAPHU only adds  $\pm 2\pi$  to the data. However, analyzing the residuals between the topographic signal present in the interferogram and the DEMs calculated by SNAPHU or EKF can indicate which DEM returns fewer fringes, thus indicating a better fit to the input DEMs. The residual fringes are shown in Fig. 14. Residuals for 080521–080730 interferogram are very similar, despite serving as input for EKF but not for SNAPHU or 3-DMLE. This suggests that EKF is able to separate the orbital effects from the DEM and is not adversely affected by the orbital errors. For all other interferograms, EKF results have fewer residual fringes; this is especially visible in interferograms 041103–050112 and 090715–090819. The interferogram 040616–040721 has the largest perpendicular baseline, and therefore the most detailed topographic signal; again, EKF residuals are significantly smaller than the SNAPHU DEM. Comparing EKF and 3-DMLE in Fig. 14 shows similar residual phase patterns. EKF residuals are sharper because of better noise suppression. The residuals for 040616–040721 interferogram obtained from the 3-DMLE algorithm are very low indicating a very good fit to the signal in that interferogram. These results show that 3-DMLE and EKF provide similar results in terms of minimizing phase residuals for this analysis.

### C. TerraSAR-X Data

For the TerraSAR-X data over Juarez-El Paso, the NED 1/9 arcsec DEM is used as benchmark, or ground truth.

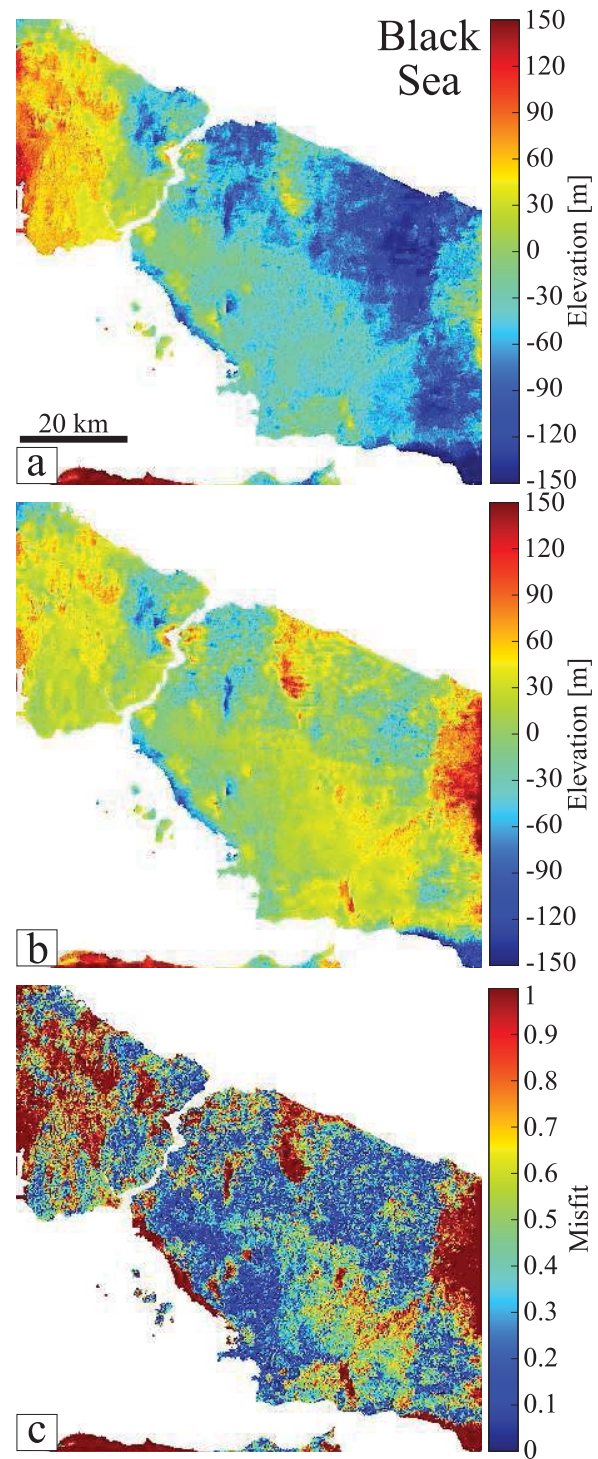


Fig. 13. Residual and misfit values for SNAPHU DEM. (a) Differences between calculated DEM and SRTM DEM. (b) Differences between detrended DEM and SRTM DEM. (c) Misfit calculated based on expected error using detrended DEM.

The NED 1/9 arcsec DEM provides bare-earth elevations, whereas the InSAR measurements are reflected from the upper layers of vegetation canopy or the top of buildings. Therefore, even though the NED 1/9 arcsec DEM is accurate to  $< 10$  cm in vertical, some misfit is expected [84]. Comparison of SRTM 3 arcsec DEM with NED 1/9 arcsec DEM indicates an rms difference of 7.5 m. The obtained rms height error in

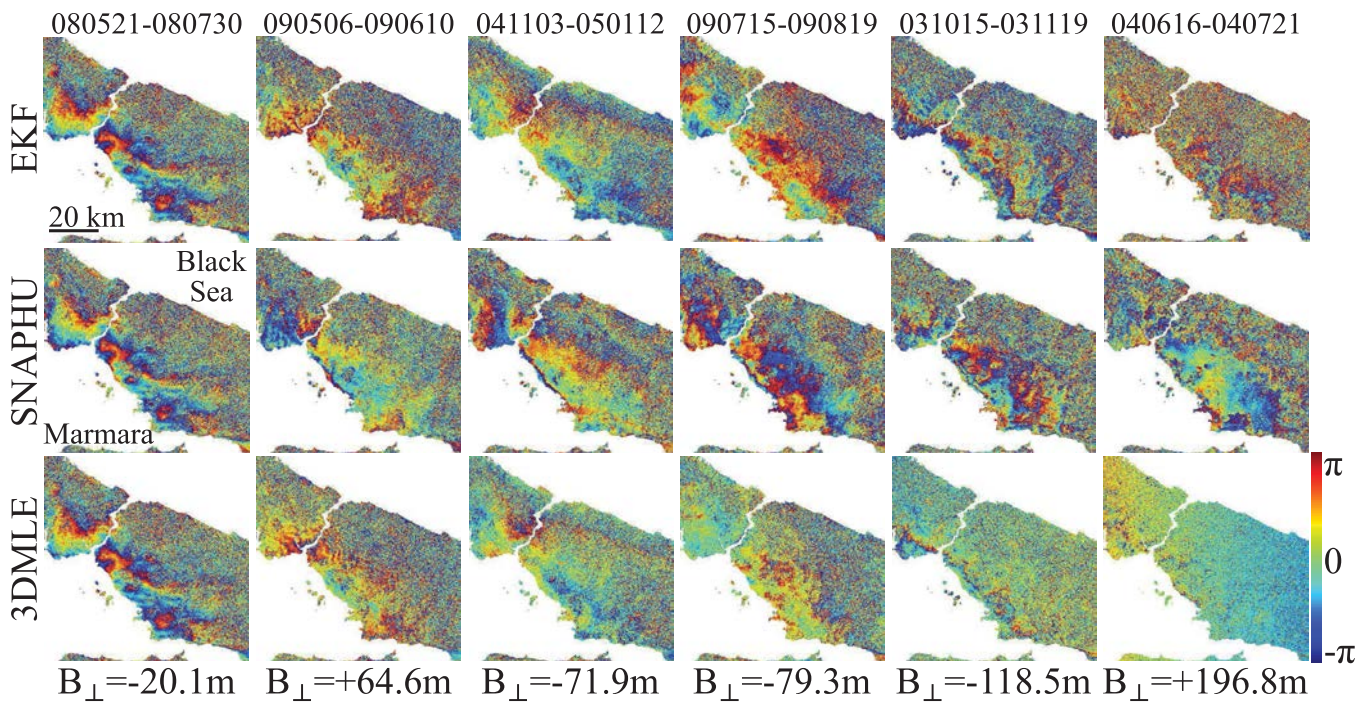


Fig. 14. Residual phase of interferograms for DEMs obtained by EKF, SNAPHU, and 3-DMLE. Top row: residuals for EKF. Middle row: residuals for SNAPHU. Bottom row: residuals for 3DMLE. Spatially correlated phase residuals: correlated DEM error.

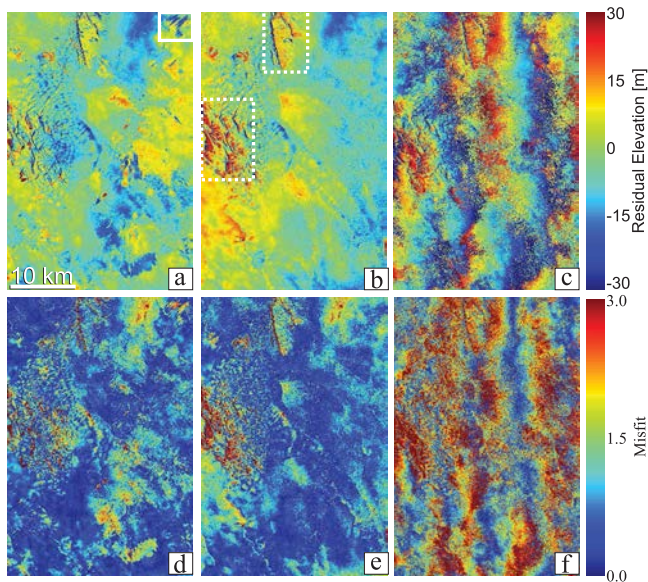


Fig. 15. Residual and misfit values for Juarez-El Paso, in comparison with NED 1/9 arcsec DEM as benchmark. (a) Residual height values for EKF DEM. (b) Residual height values for SNAPHU DEM. (c) Residual height values for 3-DMLE DEM. (d) Misfit for EKF DEM. (e) Misfit for SNAPHU DEM. (f) Misfit for 3-DMLE DEM. Linear errors are evident in EKF result as shown inside white box in (a). In (b), dashed white lines highlight mountainous areas to north and west.

comparison with the NED 1/9 arcsec DEM for 3-DMLE is 18.0, SNAPHU is 10.6, and 9.7 m for EKF. The increased rms error for all results is likely because of the difference between bare-earth elevations and InSAR-derived topography. Residuals and misfit values for EKF, SNAPHU and 3-DMLE DEMs are shown in Fig. 15 and Table II. Misfits shown

in Table II for EKF indicate 8%–18% improvement with respect to SNAPHU. EKF results are in better agreement over the mountainous areas even though some linear error features are evident because of error propagation. Although the correlated misfits indicate differences between the bare-earth NED 1/9 arcsec DEM with the InSAR derived topography, uncorrelated misfits indicate the characteristic differences between SNAPHU and EKF methods. The area of disagreement is quite different for SNAPHU and EKF results. The characteristic differences between the SNAPHU and EKF methods mainly arise from the treatment of error in the DEM generation procedure. SNAPHU-unwrapped solutions are fit to each individual interferogram before weighted averaging, whereas EKF results are fit to the complete 3-D data set, with heavier weighting on the interferograms with longer perpendicular baselines. In addition, EKF is designed for a smooth solution because of the requirement of continuous phase slope in the prediction equations, whereas the network-based unwrapping utilized in SNAPHU handles discontinuities very well. The 3-DMLE algorithm is not able to resolve the  $2\pi$  ambiguity correctly, and therefore has banding effects shown in Fig. 15(c)–(f). It is likely that the 3-DMLE algorithm would have done better with additional data, however, for the given data set it results in large residuals. In addition, the 3-DMLE algorithm applied to the data in this paper works on individual points and does not provide any constraint on congruence of neighboring values. A modified 3-DMLE algorithm that can be applied to arcs instead of points would perhaps provide a better result.

Limiting the comparison only to mountainous areas, we obtain larger differences as shown in Table II. Results indicate that even though EKF may propagate errors along the

TABLE II  
DEM RESIDUALS AND MISFITS BASED ON NED 1/9 ARCSEC FOR JUAREZ-EL PASO

Area	Residual [m]			Misfit <i>n.a.</i> <sup>1</sup>		
	EKF	SNAPHU	3-DMLE	EKF	SNAPHU	3-DMLE
Complete study area	9.7	10.6	18.0	1.2	1.3	2.2
Western Mountains (Cerro Bola)	14.9	17.4	20.6	2.1	2.4	2.8
Northern Mountains (Franklin)	18.0	22.7	22.4	2.3	2.8	2.8

<sup>1</sup> Misfit is unitless.

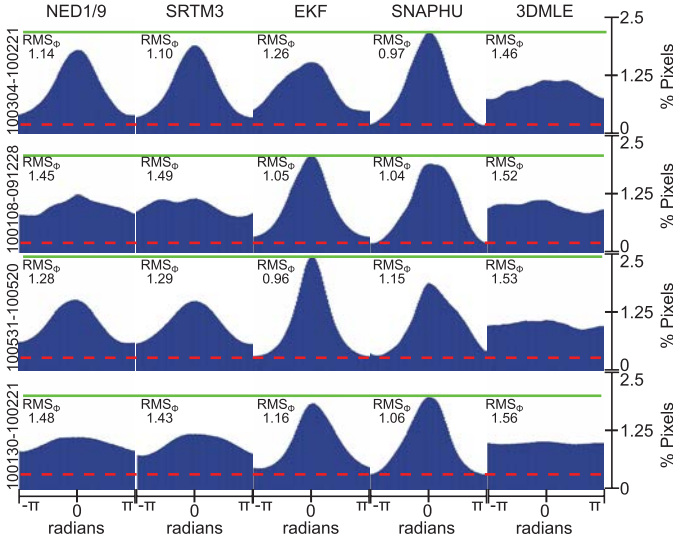


Fig. 16. Histograms of residual phase after removal of topographic signal. Each row indicates a different interferogram while each column represents different DEM. RMS phase values are presented next to each histogram. Green solid line marks highest peak and red dashed line marks the lowest tail.

unwrapping path, over mountainous areas it achieves lower rms values compared with the conventional algorithm based on SNAPHU. Both western (Cerro Bola Mt.) and northern (Franklin Mt.) mountainous areas are highlighted with a white dashed line in Fig. 15(b).

Another measure of DEM quality comes from the agreement between the calculated DEM and wrapped topographic signal in the interferograms. The main goal of this analysis is to obtain the DEM that corresponds to the topographic signal in the interferograms. When deformation, atmosphere and other noise sources are ignored, the residuals between the interferogram and the topographic signal should form a Gaussian distribution, where the mean value is a residual phase constant, and the width of the curve represents the goodness of fit. The histograms for the residual phase values are shown in Fig. 16. All histograms are shifted to have zero mean by removing the residual phase constant. Plotted histograms indicate that both the SNAPHU and EKF DEMs are better fits to the interferograms than NED 1/9 arcsec or SRTM 3 arcsec DEMs. By design, EKF gives more weight to interferograms with longer baselines, and higher coherence. This is evident in Fig. 16, where SNAPHU achieves better fit for the short baseline interferogram (100304–100221) and the long temporal baseline (lower coherence) interferogram (100130–100221). For the other two interferograms with high coherence, EKF performs better. The solid green line in Fig. 16

marks the top of the highest Gaussian, indicating the level of best fit among the data sets, whereas the dashed red line marks the lowest part of the tail, indicating the noise-floor. For the noise floor values, SNAPHU performs better in all cases except the 100531–100520 interferogram. EKF has the lowest noise floor value for 100531–100520 interferogram, which has the highest weighting in EKF, because of its high coherence and long perpendicular baseline. The histograms for residual phase distributions for 3-DMLE show uniform distribution, indicating large residuals.

## VI. CONCLUSION

In this paper, a novel 3-D unwrapping algorithm was developed and tested for generating DEMs from 3-D InSAR data. The new algorithm is based on extended Kalman filtering and combines phase filtering, unwrapping, and topography calculation in a single operation. Analysis of a synthetic data set showed stable filter characteristics over smooth terrain. The comparison of the DEMs over Istanbul, obtained by EKF, SNAPHU, and 3-DMLE showed that the path-following EKF can correctly unwrap disconnected patches of coherent areas, as long as an initial estimate is provided. The results obtained over Juarez-El Paso using TerraSAR-X data indicated that EKF algorithm can indeed improve the vertical accuracy of an input DEM to better fit topographic signal in InSAR images.

## APPENDIX

### SMOOTH SURFACE ASSUMPTION

We assume that topography is a smooth surface that can be defined as a continuously differentiable scalar field. Any scalar field has an irrotational gradient field, which is often shown with the identity

$$\nabla \times \nabla z = 0 \quad (A1)$$

where  $\nabla \times$  is curl,  $\nabla$  is the gradient operation and  $z$  is topography. Even though there are discontinuities present in the Earth's topography, for many phase unwrapping algorithms path independence of the solution is enforced by the same identity, based on the idea that the gradients of interferometric phase are equal to their unwrapped counterparts [3], [42]. Any point on a continuously differentiable scalar field can be defined using multivariate Taylor's expansion. The first-order approximation using Taylor's expansion with two variables is

$$z(x, y) = z(x_0, y_0) + (x - x_0) \frac{\partial z(x_0, y_0)}{\partial x} + (y - y_0) \frac{\partial z(x_0, y_0)}{\partial y} \quad (A2)$$

where  $z$  is topography defined over 2-D space  $(x, y)$ ,  $\partial z/\partial x$  is the partial derivative of topography for the 1-D  $(x)$ , and subscript 0 is used to indicate the coordinates of the reference point. We use this approximation to initialize the Kalman filter. The predicted topography value using this first-order Taylor's expansion will be wrong over discontinuities, or over areas where interferograms do not define a surface (low-coherence areas, i.e., water). This is why we delay the unwrapping of such areas to the end of the unwrapping operation based on Fisher's Distance.

#### ACKNOWLEDGMENT

The author would like to thank NASA for the NESSF Fellowship provided from 2007 to 2010, 09-Earth-09R-61 and Scott M. Baker for helpful discussions. The Istanbul ASAR data was provided by GEO's Geohazard Superites. The authors would like to thank DLR for providing the TerraSAR-X stripmap data over Juarez-El Paso under the science data proposal HYD0655. They would also like to thank the Department of Energy for on-going support. The authors would like to thank NASA for research grant NNX12AK23G.

#### REFERENCES

- [1] L. C. Graham, "Synthetic interferometer radar for topographic mapping," *Proc. IEEE*, vol. 62, no. 6, pp. 763–768, Jun. 1974.
- [2] H. A. Zebker and R. M. Goldstein, "Topographic mapping from interferometric synthetic aperture radar observations," *J. Geophys. Res., Solid Earth*, vol. 91, no. B5, pp. 4993–4999, 1986.
- [3] R. M. Goldstein, H. A. Zebker, and C. L. Werner, "Satellite radar interferometry: Two-dimensional phase unwrapping," *Radio Sci.*, vol. 23, no. 4, pp. 713–720, 1988.
- [4] D. C. Ghiglia and L. A. Romero, "Robust two-dimensional weighted and unweighted phase unwrapping that uses fast transforms and iterative methods," *J. Opt. Soc. Amer. A*, vol. 11, no. 1, pp. 107–117, 1994.
- [5] R. Bamler and R. Wessling, *Digital Terrain Models from Radar Interferometry* (Photogrammetric Week). Heidelberg, Germany: Wichmann Verlag, 1997, pp. 93–105.
- [6] M. Costantini, "A novel phase unwrapping method based on network programming," *IEEE Trans. Geosci. Remote Sens.*, vol. 36, no. 3, pp. 813–821, May 1998.
- [7] R. Bürgmann, P. Rosen, and E. Fielding, "Synthetic aperture radar interferometry to measure Earth's surface topography and its deformation," *Annu. Rev. Earth Planetary Sci.*, vol. 28, no. 1, pp. 169–209, 2000.
- [8] D. Massonnet and K. Feigl, "Radar interferometry and its application to changes in the Earth's surface," *Rev. Geophys.*, vol. 36, no. 4, pp. 441–500, 1998.
- [9] H. A. Zebker and J. Villasenor, "Decorrelation in interferometric radar echoes," *IEEE Trans. Geosci. Remote Sens.*, vol. 30, no. 5, pp. 950–959, Sep. 1992.
- [10] A. Ferretti, C. Prati, and F. Rocca, "Multibaseline InSAR DEM reconstruction: The wavelet approach," *IEEE Trans. Geosci. Remote Sens.*, vol. 37, no. 2, pp. 705–715, May 1999.
- [11] A. Ferretti, C. Prati, and F. Rocca, "Multibaseline phase unwrapping for InSAR topography estimation," *Nuovo Cimento Della Societa Italiana di Fisica. C. Geophys. Space Phys.*, vol. 24, no. 1, pp. 159–176, 2001.
- [12] L. Ying, D. Munson, Jr., R. Koetter, and B. Frey, "Multibaseline InSAR terrain elevation estimation: A dynamic programming approach," in *Proc. Int. Conf. Image Process.*, vol. 2, Sep. 2003, pp. 157–160.
- [13] M. Eineder and N. Adam, "A maximum-likelihood estimator to simultaneously unwrap, geocode, and fuse SAR interferograms from different viewing geometries into one digital elevation model," *IEEE Trans. Geosci. Remote Sens.*, vol. 43, no. 1, pp. 24–36, Jan. 2005.
- [14] G. Fornaro, A. Guarnieri, A. Pauciuillo, and F. De-Zan, "Maximum likelihood multi-baseline SAR interferometry," *IEE Proc. Radar Sonar Navigat.*, vol. 153, no. 3, pp. 279–288, Jun. 2006.
- [15] G. Ferraiuolo, F. Meglio, V. Pascazio, and G. Schirinzi, "DEM reconstruction accuracy in multichannel SAR interferometry," *IEEE Trans. Geosci. Remote Sens.*, vol. 47, no. 1, pp. 191–201, Jan. 2009.
- [16] H. Yu, Z. Li, and Z. Bao, "A cluster-analysis-based efficient multibaseline phase-unwrapping algorithm," *IEEE Trans. Geosci. Remote Sens.*, vol. 49, no. 1, pp. 478–487, Jan. 2011.
- [17] A. Ferretti, C. Prati, and F. Rocca, "Nonlinear subsidence rate estimation using permanent scatterers in differential SAR interferometry," *IEEE Trans. Geosci. Remote Sens.*, vol. 38, no. 5, pp. 2202–2212, Sep. 2000.
- [18] A. Ferretti, C. Prati, and F. Rocca, "Permanent scatterers in SAR interferometry," *IEEE Trans. Geosci. Remote Sens.*, vol. 39, no. 1, pp. 8–20, Jan. 2001.
- [19] B. Kampes, "Displacement parameter estimation using permanent scatterer interferometry," Ph.D. dissertation, Faculty Civil Eng. Geosci., Technische Univ. Delft, Delft, The Netherlands, 2005.
- [20] B. Kampes, *Radar Interferometry—Persistent Scatterer Technique* (Remote Sensing and Digital Image Processing), vol. 12. New York, NY, USA: Springer-Verlag, 2006.
- [21] P. Berardino, G. Fornaro, R. Lanari, and E. Sansosti, "A new algorithm for surface deformation monitoring based on small baseline differential SAR interferograms," *IEEE Trans. Geosci. Remote Sens.*, vol. 40, no. 11, pp. 2375–2383, Nov. 2002.
- [22] R. Lanari, F. Casu, M. Manzo, G. Zeni, P. Berardino, M. Manunta, and A. Pepe, "An overview of the small baseline subset algorithm: A DInSAR technique for surface deformation analysis," *Pure Appl. Geophys.*, vol. 164, no. 4, pp. 637–661, 2007.
- [23] T. Lauknes, H. Zebker, and Y. Larsen, "InSAR deformation time series using an  $L_1$ -norm small-baseline approach," *IEEE Trans. Geosci. Remote Sens.*, vol. 49, no. 1, pp. 536–546, Jan. 2011.
- [24] A. Hooper, H. Zebker, P. Segall, and B. Kampes, "A new method for measuring deformation on volcanoes and other natural terrains using InSAR persistent scatterers," *Geophys. Res. Lett.*, vol. 31, no. 23, p. 5, 2004.
- [25] A. Ferretti, F. Novali, A. Fumagalli, C. Prati, F. Rocca, and A. Rucci, "Beyond PSInSAR: The SQUEESAR approach," in *Proc. AGU Fall Meeting Abstracts*, vol. 1, 2009, p. 2.
- [26] M. Kim and H. Griffiths, "Phase unwrapping of multibaseline interferometry using Kalman filtering," in *Proc. 7th Int. Conf. Image Process. Appl.*, vol. 2, 1999, pp. 813–817.
- [27] J. M. Huntley, "Three-dimensional noise-immune phase unwrapping algorithm," *Appl. Opt.*, vol. 40, no. 23, pp. 3901–3908, Aug. 2001.
- [28] R. Cusack and N. Papadakis, "New robust 3-D phase unwrapping algorithms: Application to magnetic field mapping and undistorting echoplanar images," *Neuroimage*, vol. 16, no. 3, pp. 754–764, 2002.
- [29] M. Costantini, F. Malvarosa, F. Minati, L. Pietranera, and G. Milillo, "A three-dimensional phase unwrapping algorithm for processing of multitemporal SAR interferometric measurements," in *Proc. IEEE Int. Geosci. Remote Sens. Symp.*, vol. 3, Jun. 2002, pp. 1741–1743.
- [30] M. Jenkinson, "Fast, automated, n-dimensional phase-unwrapping algorithm," *Magn. Resonance Med.*, vol. 49, no. 1, pp. 193–197, 2003.
- [31] H. Abdul-Rahman, M. Gdeisat, D. Burton, M. Lalor, F. Lilley, and C. Moore, "Fast and robust three-dimensional best path phase unwrapping algorithm," *Appl. Opt.*, vol. 46, no. 26, pp. 6623–6635, 2007.
- [32] A. Hooper and H. A. Zebker, "Phase unwrapping in three dimensions with application to InSAR time series," *J. Opt. Soc. Amer. A*, vol. 24, no. 9, pp. 2737–2747, 2007.
- [33] A. Hooper, "A statistical-cost approach to unwrapping the phase of InSAR time series," in *Proc. ESA FRINGE Workshop*, Frascati, Italy, Nov.–Dec. 2009.
- [34] M. Costantini, F. Malvarosa, and F. Minati, "A novel approach for redundant integration of finite differences and phase unwrapping on a sparse multidimensional domain," in *Proc. IEEE Int. Geosci. Remote Sens. Symp.*, Jul. 2010, pp. 1565–1568.
- [35] G. Fornaro, A. Pauciuillo, and D. Reale, "A null-space method for the phase unwrapping of multitemporal SAR interferometric stacks," *IEEE Trans. Geosci. Remote Sens.*, vol. 49, no. 6, pp. 2323–2334, Jun. 2011.
- [36] A. Ferretti, C. Prati, F. Rocca, and A. Monti Guarnieri, "Multibaseline SAR interferometry for automatic DEM reconstruction," in *Proc. 3rd ERS Symp. Space Service Environ.*, vol. 414, 1997, pp. 1809–1820.
- [37] V. Pascazio and G. Schirinzi, "Estimation of terrain elevation by multi-frequency interferometric wide band SAR data," *IEEE Signal Process. Lett.*, vol. 8, no. 1, pp. 7–9, Jan. 2001.

- [38] V. Pascazio and G. Schirinzì, "Multifrequency InSAR height reconstruction through maximum likelihood estimation of local planes parameters," *IEEE Trans. Image Process.*, vol. 11, no. 12, pp. 1478–1489, Dec. 2002.
- [39] G. Ferraiuolo, V. Pascazio, and G. Schirinzì, "Maximum a posteriori estimation of height profiles in InSAR imaging," *IEEE Geosci. Remote Sens. Lett.*, vol. 1, no. 2, pp. 66–70, Apr. 2004.
- [40] G. Fornaro, A. Pauciuolo, and E. Sansosti, "Phase difference-based multichannel phase unwrapping," *IEEE Trans. Image Process.*, vol. 14, no. 7, pp. 960–972, Jul. 2005.
- [41] T. Farr, P. Rosen, E. Caro, R. Crippen, R. Duren, S. Hensley, M. Kobrick, M. Paller, E. Rodriguez, L. Roth, D. Seal, S. Shaffer, J. Shimada, J. Umland, M. Werner, M. Oskin, D. Burbank, and D. Alsdorf, "The shuttle radar topography mission," *Rev. Geophys.*, vol. 45, no. 2, pp. 583–585, Jun. 2007.
- [42] R. Bamler and P. Hartl, "Synthetic aperture radar interferometry," *Inverse Problems*, vol. 14, no. 4, pp. R1–R54, 1998.
- [43] R. F. Hanssen, *Radar Interferometry: Data Interpretation and Error Analysis*. Norwell, MA, USA: Kluwer, 2001.
- [44] D. Small, P. Pasquali, and S. Fuglistaler, "A comparison of phase to height conversion methods for SAR interferometry," in *Proc. Int. Geosci. Remote Sens. Symp., Remote Sens. Sustainable Future*, vol. 1, May 1996, pp. 342–344.
- [45] R. Krämer, "Auf Kalman-Filtern basierende phasen- und parameterestimation zur lösung der phasenvieldeutigkeitsproblematik bei der höhenmodellierung aus SAR-interferogrammen." Ph.D. dissertation, Dept. Zentrum for Sensorsysteme (ZESS), Universitat-GH Siegen, Siegen, Germany, 1998.
- [46] J. M. N. Leitaó and M. A. T. Figueiredo, "Absolute phase image reconstruction: A stochastic nonlinear filtering approach," *IEEE Trans. Image Process.*, vol. 7, no. 6, pp. 868–882, Jun. 1998.
- [47] O. Loffeld, H. Nies, S. Knedlik, and Y. Wang, "Phase unwrapping for SAR interferometry—A data fusion approach by Kalman filtering," *IEEE Trans. Geosci. Remote Sens.*, vol. 46, no. 1, pp. 47–58, Jan. 2008.
- [48] H. Nies, O. Loffeld, and R. Wang, "Phase unwrapping using 2D-Kalman filter—potential and limitations," in *Proc. IEEE Int. Geosci. Remote Sens. Symp.*, vol. 4, Jul. 2008, pp. IV-1213–IV-1216.
- [49] J. Martinez-Espla, T. Martinez-Marin, and J. Lopez-Sanchez, "A particle filter approach for InSAR phase filtering and unwrapping," *IEEE Trans. Geosci. Remote Sens.*, vol. 47, no. 4, pp. 1197–1211, Apr. 2009.
- [50] D. Willner, C. B. Chang, and K. P. Dunn, "Kalman filter algorithms for a multi-sensor system," in *Proc. IEEE Conf. Decision Control, 15th Symp. Adapt. Process.*, vol. 15, Dec. 1976, pp. 570–574.
- [51] Q. Gan and C. Harris, "Comparison of two measurement fusion methods for Kalman-filter-based multisensor data fusion," *IEEE Trans. Aerosp. Electron. Syst.*, vol. 37, no. 1, pp. 273–279, Jan. 2001.
- [52] J. Roecker and C. McGillem, "Comparison of two-sensor tracking methods based on state vector fusion and measurement fusion," *IEEE Trans. Aerosp. Electron. Syst.*, vol. 24, no. 4, pp. 447–449, Jul. 1988.
- [53] S. Sun and Z. Deng, "Multi-sensor optimal information fusion Kalman filter," *Automatica*, vol. 40, no. 6, pp. 1017–1023, 2004.
- [54] S. J. Julier, "A new extension of the Kalman filter to nonlinear systems," *Int. Symp. Aerosp., Defense Sens., Simul. Controls*, vol. 3, 1997, pp. 182–193.
- [55] E. Wan and R. Van Der Merwe, "The unscented Kalman filter for nonlinear estimation," in *Proc. IEEE Adapt. Syst. Signal Process., Commun., Control Symp.*, Oct. 2000, pp. 153–158.
- [56] S. Haykin, *Kalman Filtering And Neural Networks*. New York, NY, USA: Wiley, 2001.
- [57] R. van der Merwe, N. de Freitas, A. Doucet, and E. Wan, "The unscented particle filter," Dept. Eng., Cambridge Univ., Cambridge, U.K., Tech. Rep. CUED/F-INENG/TR 380, Aug. 2000.
- [58] R. E. Kalman, "A new approach to linear filtering and prediction problems," *ASME J. Basic Eng.*, vol. 82, no. 1, pp. 35–45, 1960.
- [59] P. S. Maybeck, *Stochastic Models, Estimation, and Control: Introduction*. New York, NY, USA: Academic, 1979, ch. 1.
- [60] G. Welch and G. Bishop, "An introduction to the Kalman filter," Dept. Comput. Sci., Univ. North Carolina, Chapel Hill, NC, USA, Tech. Rep. TR 95-041, 1995.
- [61] J. Lee, L. Jurkevich, P. Dewaele, P. Wambacq, and A. Oosterlinck, "Speckle filtering of synthetic aperture radar images: A review," *Remote Sens. Rev.*, vol. 8, no. 4, pp. 313–340, 1994.
- [62] J. M. Bioucas-Dias and J. Leitaó, "InSAR phase unwrapping: A Bayesian approach," in *Proc. IEEE Int. Geosci. Remote Sens. Symp.*, vol. 1, Jul. 2001, pp. 396–400.
- [63] F. Lombardini, F. Gini, and P. Matteucci, "Application of array processing techniques to multibaseline InSAR for layover solution," in *Proc. IEEE Radar Conf.*, May 2001, pp. 210–215.
- [64] A. Ferretti, A. Monti-Guarnieri, C. Prati, F. Rocca, and D. Massonet, *InSAR Principles-Guidelines for SAR Interferometry Processing and Interpretation*, vol. 19. Noordwijk, The Netherlands: ESA, 2007.
- [65] B. Osmanoglu, T. H. Dixon, S. Wdowinski, and E. Cabral-Cano, "On the importance of path for phase unwrapping in synthetic aperture radar interferometry," *Appl. Opt.*, vol. 50, no. 19, pp. 3205–3220, 2011.
- [66] D. Just and R. Bamler, "Phase statistics of interferograms with applications to synthetic aperture radar," *Appl. Opt.*, vol. 33, no. 20, pp. 4361–4368, 1994.
- [67] M. Pritt, "Phase unwrapping by means of multigrid techniques for interferometric SAR," *IEEE Trans. Geosci. Remote Sens.*, vol. 34, no. 3, pp. 728–738, May 1996.
- [68] D. C. Ghiglia and M. D. Pritt, *Two-Dimensional Phase Unwrapping: Theory, Algorithms and Software*. New York, NY, USA: Wiley, May 1998.
- [69] Z. Zhang, "Parameter estimation techniques: A tutorial with application to conic fitting," *Image Vis. Comput.*, vol. 15, no. 1, pp. 59–76, 1997.
- [70] M. Crosetto, "Calibration and validation of SAR interferometry for DEM generation," *ISPRS J. Photogram. Remote Sens.*, vol. 57, no. 3, pp. 213–227, 2002.
- [71] C. W. Chen and H. A. Zebker, "Two-dimensional phase unwrapping with use of statistical models for cost functions in nonlinear optimization," *J. Opt. Soc. Amer. A*, vol. 18, no. 2, pp. 338–351, 2001.
- [72] C. W. Chen, "Statistical-cost network-flow approaches to two-dimensional phase unwrapping for radar interferometry," Ph.D. dissertation, Dept. Electr. Eng., Stanford Univ., Stanford, CA, USA, Jun. 2001.
- [73] J. Eaton, *GNU Octave Manual*. Bristol, U.K.: Network Theory Ltd., 2008.
- [74] S. Akarvardar, K. Feigl, and S. Ergintav, "Ground deformation in an area later damaged by an earthquake: Monitoring the Avcilar district of Istanbul, Turkey, by satellite radar interferometry 1992–1999," *Geophys. J. Int.*, vol. 178, no. 2, pp. 976–988, 2009.
- [75] T. R. Walter, M. Manzo, A. Manconi, G. Solaro, R. Lanari, M. Motagh, H. Woith, S. Parolai, M. Shirzaei, J. Zschau, S. Baris, and A. Ansal, "Satellite monitoring of hazards: A focus on Istanbul, Turkey," *EOS, Trans., Amer. Geophys. Union*, vol. 91, no. 36, pp. 313–324, Sep. 2010.
- [76] P. Willis, C. Jayles, and Y. Bar-Sever, "DORIS: From orbit determination for altimeter missions to geodesy," *Comptes Rendus Geosci.*, vol. 338, nos. 14–15, pp. 968–979, 2006.
- [77] European Space Agency. (2011). *Doris Precise Orbit State Vectors (dor\_vor\_ax)*, Paris, France [Online]. Available: <http://earth.esa.int/object/index.cfm?objectId=1502>
- [78] C. W. Chen and H. A. Zebker, "Network approaches to two-dimensional phase unwrapping: Intractability and two new algorithms," *J. Opt. Soc. Amer. A*, vol. 17, no. 3, pp. 401–414, 2000.
- [79] C. W. Chen and H. A. Zebker, "Phase unwrapping for large SAR interferograms: Statistical segmentation and generalized network models," *IEEE Trans. Geosci. Remote Sens.*, vol. 40, no. 8, pp. 1709–1719, Aug. 2002.
- [80] B. Kampes and S. Usai, "DORIS: The delft object-oriented radar interferometric software," in *Proc. 2nd Int. Symp. Operationalization Remote Sens.*, 1999, pp. 1–4.
- [81] S. Hong, S. Wdowinski, S. Kim, and J. Won, "Multi-temporal monitoring of wetland water levels in the florida everglades using interferometric synthetic aperture radar (InSAR)," *Remote Sens. Environ.*, vol. 114, no. 11, pp. 2436–2447, 2010.
- [82] J. Mittermayer, B. Schattler, and M. Younis, "TerraSAR-X commissioning phase execution and results," in *Proc. IEEE Int. Geosci. Remote Sens. Symp.*, vol. 2, Jul. 2008, pp. 197–200.
- [83] Y. Yoon, M. Eineder, N. Yague-Martinez, and O. Montenbruck, "TerraSAR-X precise trajectory estimation and quality assessment," *IEEE Trans. Geosci. Remote Sens.*, vol. 47, no. 6, pp. 1859–1868, Jun. 2009.
- [84] *Juarez, Mexico District and El Paso County, Texas Border area, October 2007 and January 2008, 1/9-arc Second National Elevation Dataset*, USGS, Reston, VA, USA, Jan. 2009.

- [85] B. Rabus, M. Eineder, A. Roth, and R. Bamler, "The shuttle radar topography mission—A new class of digital elevation models acquired by spaceborne radar," *ISPRS J. Photogram. Remote Sens.*, vol. 57, no. 4, pp. 241–262, 2003.
- [86] H. Reuter, A. Nelson, P. Strobl, W. Mehl, and A. Jarvis, "A first assessment of Aster GDEM tiles for absolute accuracy, relative accuracy and terrain parameters," in *Proc. IEEE Int. Geosci. Remote Sens. Symp.*, vol. 5, Jul. 2009, pp. V-240–V-243.
- [87] C. Hirt, M. Filmer, and W. Featherstone, "Comparison and validation of recent freely-available ASTER-GDEM ver 1, SRTM ver 4. 1 and GEODATA DEM-9S ver 3 digital elevation models over Australia," *Austral. J. Earth Sci.*, vol. 57, no. 3, pp. 337–347, 2010.
- [88] G. Krieger, A. Moreira, H. Fiedler, I. Hajnsek, M. Werner, M. Younis, and M. Zink, "TanDEM-X: A satellite formation for high-resolution SAR interferometry," *IEEE Trans. Geosci. Remote Sens.*, vol. 45, no. 11, pp. 3317–3341, Nov. 2007.
- [89] E. Rodriguez, C. Morris, and J. Belz, "A global assessment of the SRTM performance," *Photogram. Eng. Remote Sens.*, vol. 72, no. 3, pp. 249–260, 2006.
- [90] N. Yastıklı, G. Koçak, and G. Büyüksalih, "Accuracy and morphological analyses of GTOPO30 and SRTM X-C band DEMs in the test area Istanbul," in *Proc. ISPRS Topograph. Mapping Space Workshop*, Feb. 2006, pp. 1–6.



**Batuhan Osmanoglu** received the B.Sc. degree in telecommunications engineering from Istanbul Technical University, Istanbul, Turkey, in 2005, and the Ph.D. degree in marine geology and geophysics from the University of Miami, Miami, FL, USA, in 2011. His doctoral research focused on synthetic aperture radar interferometry time series analysis.

He is currently a Post-Doctoral Fellow with the University of Alaska-Fairbanks, Fairbanks, AK, USA, where he is remotely measuring surface velocities of glaciers in Antarctica. He is specialized in

detecting land motion using radar imaging satellites. His current research interests include all aspects of radar remote sensing, and he has worked on applications for observing earth surface deformation, measuring target velocities, and boosting signal-to-noise ratio in target detection algorithms.

Dr. Osmanoglu is the Co-Founder and partner of BOS Technologies, LLC. He helps to create new features for TU-Delft's DORIS software and he is the lead developer of the Automated DORIS Environment. He is the acting Co-Chair for ISPRS VII/WG7 Synergy in radar and lidar work group and the Natural Sciences Committee of Turkish American Scientists and Scholars Association.



**Tim Dixon** received the B.Sc. degree from the University of Western Ontario, London, ON, Canada, in 1974, and the Ph.D. degree from the University of California at San Diego, San Diego, CA, USA.

He was with NASA's Jet Propulsion Laboratory, n Pasadena, CA, from 1979 to 1992. He was a Professor with the University of Miami, Coral Gables, FL, USA, from 1992 to 2010, where he co-founded the Center for Southeastern Tropical Advanced Remote Sensing. Since January 2011, he has been with the University of South Florida, Tampa, FL, where he is currently a Professor with the Department of Geology. He was a Distinguished Lecturer for the American Association of Petroleum Geologists from 2006 to 2007. His current research interests include the use of microwave techniques to study earthquakes and volcano deformation, coastal subsidence, groundwater extraction, and glacier motion.

Dr. Dixon is a fellow of the American Geophysical Union and the Geological Society of America (GSA). He was a recipient of the GSA "Best Paper" Award in 2006, and the GSA's Woollard Award in 2010.



**Shimon Wdowinski** received the B.Sc. degree in earth sciences and the M.Sc. degree in geology from the Hebrew University, Jerusalem, Israel, in 1983 and 1985, respectively, and the M.S. degree in engineering sciences and the Ph.D. degree in geophysics from Harvard University, Boston, MA, USA, in 1988 and 1990, respectively.

He is currently a Research Associate Professor with the Division of Marine Geology and Geophysics, Rosenstiel School of Marine and Atmospheric Science, University of Miami, Coral

Gables, FL, USA. He is a Principal Investigator of projects funded by NASA, ESA, Canadian Space Agency, German Space Agency, and Italian Space Agency on studies using SAR and InSAR observations for wetland research. His current research interests include the development and usage of space geodetic techniques that can detect very precisely small movements on the Earth's surface. He successfully applied these technologies to study natural hazards and environmental phenomena, such as earthquakes, sea-level rise, landslides, urban subsidence, and wetland surface flow.